Ashwal, L. D., Ziegler, A., Glynn, S., Truebody, T., Bolhar, R. (2021): Sr-Enriched Glassy Picrites From the Karoo Large Igneous Province are Evolved, not Primitive Magmatic Rocks. - Geochemistry Geophysics Geosystems (G3), 22, 4, e2020GC009561.

https://doi.org/10.1029/2020GC009561

Geochemistry, Geophysics, Geosystems

RESEARCH ARTICLE
10.1029/2020GC009561

Special Section:
Africa plate geosystems

Sr-Enriched Glassy Picrites From the Karoo Large Igneous Province are Evolved, not Primitive Magmatic Rocks

Lewis D. Ashwal[1], Alexander Ziegler[2], Sarah Glynn[1,3], Tristan Truebody[1,4], and Robert Bolhar[1]

[1]School of Geosciences, University of the Witwatersrand, Johannesburg, South Africa, [2]Microscopy and Microanalysis Unit, University of the Witwatersrand, Johannesburg, South Africa, [3]GFZ German Research Centre for Geosciences, Potsdam, Germany, [4]Now at Amatshe Mining, Johannesburg, South Africa

Key Points:

- Microbeam measurements in six incompatible element-rich Karoo picrites show the glasses to be the repositories for K, Sr, Ba, Zr, and H_2O
- Glasses formed by fractional crystallization of olivine, pyroxene, ilmenite, and apatite from enriched melts derived from mantle lithosphere
- The alkali picrites are mixtures of accumulated olivine phenocrysts and evolved residual melts, and do not represent primitive magmatic rocks

Supporting Information:

Supporting Information may be found in the online version of this article.

Correspondence to:

L. D. Ashwal,
lewis.ashwal@wits.ac.za

Citation:

Ashwal, L. D., Ziegler, A., Glynn, S., Truebody, T., & Bolhar, R. (2021). Sr-enriched glassy picrites from the Karoo Large Igneous Province are evolved, not primitive magmatic rocks. *Geochemistry, Geophysics, Geosystems*, *22*, e2020GC009561. https://doi.org/10.1029/2020GC009561

Received 25 NOV 2020
Accepted 26 FEB 2021

Abstract Magmatic products of the Karoo Large Igneous Province can be divided into a volumetrically dominant, compositionally uniform low-Ti tholeiitic suite, and a subordinate, geographically restricted, compositionally diverse, incompatible-rich high-Ti suite. High-Ti picrites contain up to 2,400 ppm Sr, 1,900 ppm Ba, and 550 ppm Zr, which seems unusual for olivine-enriched rocks. We studied six Karoo picrites to determine the phase(s) in which Sr resides. Samples consist of 10–30% olivine phenocrysts in a groundmass of brown glass, augite, feldspar, ilmenite, and apatite. Glass compositions vary, but are generally evolved, ranging from basaltic trachyandesite to dacite. X-ray intensity maps demonstrate that most of the Sr resides in the glasses, and to a lesser extent, in feldspars, if present. Some samples contain two texturally and compositionally distinct glasses, best modeled in terms of magma hybridization: variably accumulated olivine phenocrysts surrounded by evolved Sr-rich (to 9,470 ppm) Type 2 melts formed by extensive olivine fractionation were infiltrated by chemically distinct Type 1 melts. Upon eruption, Type 2 melt quenched to minor glass around olivine phenocrysts, and the dominant Type 1 glass acquired its evolved composition by quench crystallization of groundmass mineral phases. Both glasses are rich in H_2O (up to 3.8 wt. %) but are nearly devoid of CO_2. Calculated parental melts have much higher K_2O and incompatible trace elements (e.g., Sr or Ba >1,200 ppm) relative to low-Ti tholeiites. The unusual parental melt compositions imply derivation by small degrees of partial melting from SCLM mantle sources enriched in Sr and other incompatibles.

Plain Language Summary Rocks rich in the mineral olivine should contain only small amounts of elements unable to be accommodated in its crystal structure. But picrites from the Jurassic Karoo Large Igneous Province in southern Africa are extraordinarily enriched in K, Sr, Ba, Zr, and P. We used microbeam instruments to locate the repositories of these elements in six picrite samples, and found that they are highly concentrated in the glasses that formed as the magmas were quenched near the Earth's surface after having ascended from deeper levels. The glasses represent residual melts after extensive earlier precipitation of mineral phases during fractional crystallization. Elements excluded from the minerals became concentrated in residual melts and eventually quenched to form glass. Calculated original parental melt compositions for the picrites have much higher K, Sr, Ba, Zr, and other "incompatible elements" relative to the vast majority of Karoo basaltic melts. This implies that magmas parental to the picrites were derived by partial melting of small regions in the Earth's mantle that are unusually enriched in such elements, at depths of a few hundred kilometers. This implies a possible link between the Karoo picrites and kimberlites, which have similar chemical features and mantle sources.

1. Introduction

In his pioneering work on the Karoo region of southern Africa, Keith Cox recognized that the mafic magmatic rocks of continental flood basalt provinces, now associated with Large Igneous Provinces (LIPs), are divisible into two distinct geochemical types, one with unusual enrichments in K, Ti, P, Ba, Sr, and Zr, and another with more "normal" tholeiitic compositions (Cox et al., 1965, 1967). This distinction, frequently designated as high-Ti vs. low-Ti suites, has been corroborated for Karoo flows, sills, and dikes by numerous subsequent studies (e.g., Duncan et al., 1984; Jourdan et al., 2007), and successfully applied to many other continental flood basalt provinces including the Deccan (Cox & Hawkesworth, 1985; Melluso et al., 2004),

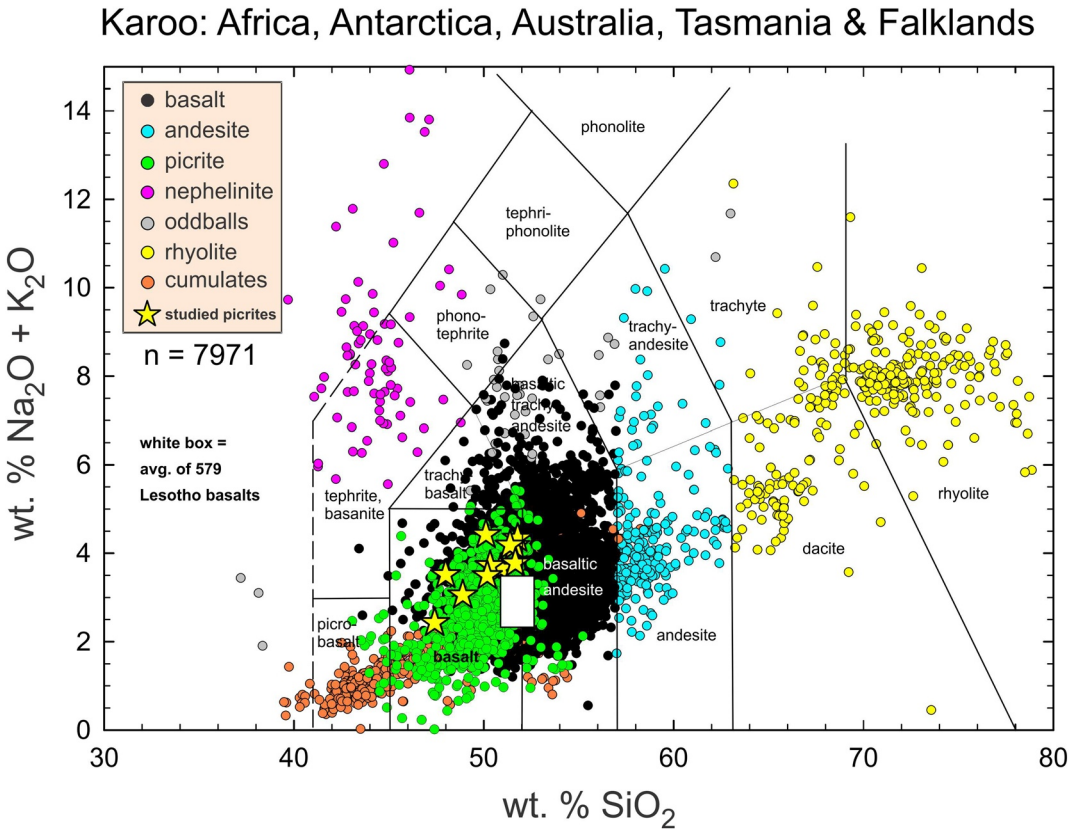

Figure 1. Total alkalies vs. silica (TAS) diagram showing compilation of 7,971 whole rock major element analyses of Karoo magmatic rocks from South Africa, Lesotho, Eswatini (formerly Swaziland), Zimbabwe, Botswana, Mozambique, Namibia, Antarctica, Australia, Tasmania, and the Falkland Islands. Data sources: Duncan et al. (1984) database (n = 4,251), GEOROC database (n = 1,868), published papers (n = 1,575), unpublished data of J.S. Marsh (n = 277). The vast volumetric majority of Karoo mafic rocks are low-Ti tholeiites, which almost entirely plot inside the white box, representing the average of 579 Lesotho basalts (1σ standard deviation). We have excluded the low-Ti Karoo sills and dikes from our average because these intrusives cooled more slowly than the lavas, and may have experienced some mineral accumulation. In contrast, the high-Ti rock suite is extremely compositionally variable, but has been over-sampled and over-analyzed, out of proportion to its volume. Compositions of the six high-Ti alkali picrites studied in this paper (yellow stars, some samples were reanalyzed) exceed the chemical variability of the low-Ti suite of tholeiitic basalts. Karoo picritic rocks (green symbols), defined as having >12 wt. % MgO, are themselves compositionally variable, with $Na_2O + K_2O$ up to 5.4 wt. %. Note that a large number of basaltic rocks, defined as having SiO_2 = 45–57 wt. % and MgO < 10 wt. % (black symbols), plot underneath the symbols for picrites, which are highlighted in this diagram. Samples designated as "oddballs" include shoshonite, nordmarkite, and lamprophyre.

Paraná-Etendeka (Gibson et al., 1995; Peate et al., 1992), and Siberian Traps (Fedorenko et al., 1996; Hawkesworth et al., 1995) LIPs. The low-Ti suite is typically volumetrically predominant, and consists of compositionally uniform tholeiitic rocks, whereas the smaller volumes of high-Ti suite rocks are extraordinarily diverse, including basalts, picrites, andesites, nephelinites, lamproites, and a variety of other unusual lithologies (Figure 1). The two suites commonly show geographic provinciality (Figure 2), a feature readily apparent for the Karoo LIP (Cox et al., 1967; Luttinen, 2018), as well as for several other continental LIPs (Natali et al., 2017), but there is little consensus as to whether the geochemical differences reflect distinct mantle sources, degrees or depths of partial melting, and/or crustal contamination effects (e.g., Jourdan et al., 2007, and references therein). It is evident from Figure 2 that Ti concentration alone is not a flawless discriminator of the two geochemical suites, as some samples are "transitional"; some workers have shown the effectiveness of trace element abundances and/or ratios (e.g., Nb, Zr/Y) as distinguishing parameters for magma suites in the Karoo and other LIPs (e.g., Luttinen, 2018; Marsh et al., 2001).There is a substantial and growing body of literature on continental as well as oceanic LIPs, summarized in several books (Ernst, 2014; Macdougall, 1988; Mahoney & Coffin, 1997).

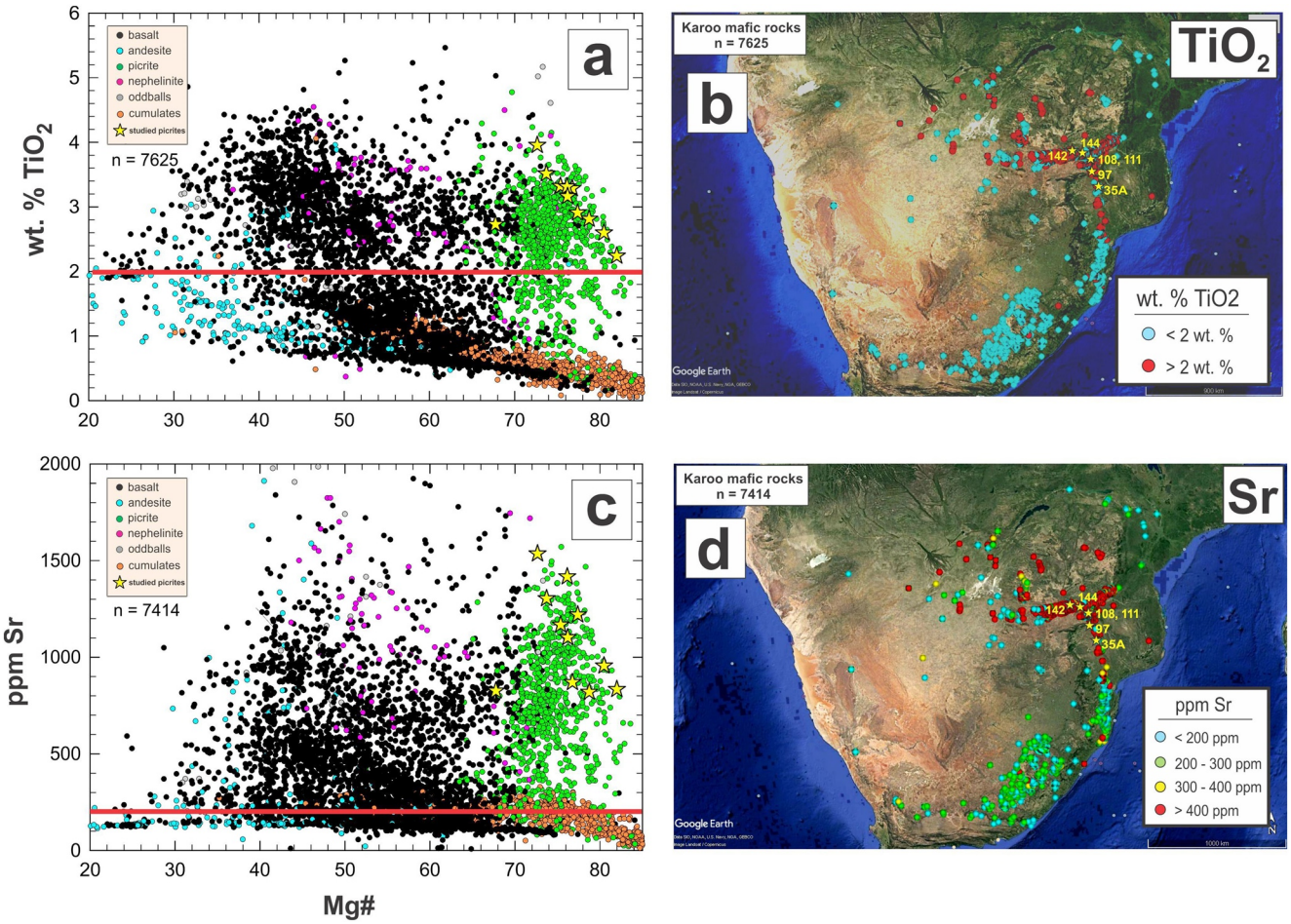

Figure 2. Left panel: Plots of Mg# vs. wt. % TiO_2 (a) and ppm Sr (c) for Karoo mafic rocks (felsic rocks such as rhyolite and dacite are omitted). Compositions of the six alkali picrites studied in this paper are shown as yellow stars (some samples were reanalyzed). Horizontal red lines separate the high-Ti and low-Ti rock suites, commonly chosen at TiO_2 = 2 wt. % and Sr = 200 ppm. Right panel: Google Earth images of southern Africa showing locations of Karoo mafic rocks color-coded according to wt. % TiO_2 (b) and ppm Sr (d). Locations of our samples, with sample numbers, are shown as yellow stars. High-Ti suite rocks are mainly concentrated in the arms of three intersecting dike swarms and linear belts of lavas in the Lebombo-Mwenezi, Sabi, and Tuli regions.

We have compiled whole rock major, trace element, and isotopic data for the Karoo LIP; the resulting database now includes nearly 8,000 entries for occurrences in South Africa, Lesotho, Eswatini (formerly Swaziland), Zimbabwe, Botswana, Mozambique, Namibia, Antarctica, Australia, Tasmania, and the Falkland Islands (Figure 1, references in caption). An intriguing feature is that the high-Ti suite of Karoo mafic extrusive and intrusive rocks includes picrites (defined as having >12 wt. % MgO) with remarkable enrichments in large-ion lithophile elements (LILE): up to 1,900 ppm Ba, 2,400 ppm Sr, 550 ppm Zr, 3,800 ppm P, and 4.8 wt. % each of K_2O and TiO_2 (Figure 2), which seems perplexing for such olivine-rich lithologies that are commonly perceived as some of the most primitive of melts in the Karoo LIP. In this paper, we report detailed mineralogical, geochemical, and textural measurements and observations of six glassy Karoo picrites, aimed at determining the phase(s) hosting the LILE, characterizing the compositionally diverse interstitial glasses, and constraining the magmatic evolution and petrogenesis of these rocks, including their mantle sources. Our approach uses mass-balance calculations and fractional crystallization modeling. The results call into question the notion that these picritic rocks are petrogenetically "primitive."

2. Geological Setting

The Karoo LIP includes mafic to felsic magmatic rocks, variably exposed over an area of 2–3 × 10^6 km^2, principally in southern Africa, but with correlatives documented in Antarctica (western Dronning Maud Land and Ferrar Province), Australia, and South America (Cox, 1988; Erlank, 1984 and papers therein; Harris et al., 1990; Luttinen & Furnes, 2000; Luttinen et al., 2010; Marsh et al., 1997; Riley et al., 2005). The magmas were emplaced rapidly over a 2–3 m.y. period in the Early Jurassic (181–184 Ma) (Jourdan et al., 2008; Svensen et al., 2012), and have been widely linked to the impingement of a deep mantle plume into Precambrian continental lithosphere, which may have initiated the break-up of the Gondwana supercontinent (Buiter & Torsvik, 2014; Storey, 1995; Storey & Kyle, 1997). Magmatic products include erosional remnants of mainly basaltic lavas (reaching ~1.5-km thick in Lesotho) and networks of dikes and sill complexes, variably exposed over an area of at least 1 × 10^6 km^2 in southern Africa and elsewhere (Figure 2). The LILE-enriched high-Ti suite of magmatic rocks is restricted mainly to the arms of three intersecting dike swarms and linear belts of lavas, interpreted as a triple junction, the center of which may represent the impingement site of the Karoo plume (e.g., Ernst & Buchan, 1997). Magma volumes are difficult to constrain with certainty because of extensive erosion and poor exposure, but we estimate there to have been at least 2–3 × 10^6 km^3, with the vast majority represented by low-Ti suite tholeiites (80–90%), and far lesser volumes (10–20%) of assorted high-Ti suite magmatic rocks. It seems apparent that the high-Ti suite has been over-sampled and over-analyzed, out of proportion to its volume (Figures 1 and 2).

The Karoo high-Ti picritic rocks, including the samples we studied, show enormous chemical variability relative to the notably more homogeneous, geographically widespread, low-Ti tholeiitic basalts as represented by the thick lava sequences in Lesotho (e.g., Marsh et al., 1997). This is illustrated in a TAS diagram (Figure 1), in which the picritic rocks (n = 897) show much larger ranges in SiO_2 and Na_2O + K_2O than the Lesotho tholeiites (n = 579). The chemical variability of the picritic rocks relative to the tholeiites is reflected in their overall higher standard deviations of averages, which extends to all major and trace elements (Table 1). Picrites are enriched by factors of 2–4 relative to tholeiites in all incompatible trace elements. The only exceptions are the HREE, which are 2–3 times higher in the tholeiites, owing to their flatter overall REE patterns (Table 1).

3. Sampling and Methodology

Thin section chips of six Karoo high-Ti suite picritic lavas, representing samples collected and studied by Bristow (1980, 1984), were provided by Chris Harris, University of Cape Town. The picrites are all from the Letaba Formation in the northern Lebombo—Mwenezi (formerly Nuanetsi) region, near the South Africa—Zimbabwe border (Figure 2). The Letaba Formation, dominated by picritic lavas, is up to 4-km thick, and is conformably underlain by nephelinites of the Mashkiri Formation (Cleverly & Bristow, 1979). GPS coordinates of our samples are given in Table 1, along with whole rock major and trace element chemical analyses from Bristow (1980) and Kamenetsky et al. (2017), who reanalyzed five of the same samples. Our samples show the following compositional ranges: MgO = 11.5–21.3 wt. %, TiO_2 = 2.6–4.0 wt. %, Sr = 826–1,536 ppm, Ba = 667–1,320 ppm, and Zr = 302–587 ppm (Table 1). The chemical variability of these six samples exceeds that of the 579 Lesotho tholeiitic basalts constituting the dominant volume of Karoo magmas (Figure 1 and Table 1). Standard polished thin sections were prepared and were used for all analytical data acquired in this study. Petrographically estimated modal abundances are given in Table 2.

Quantitative electron microprobe analyses of the major constituent phases-glasses, olivine, clinopyroxene, Cr-rich and Cr-poor spinel, and ilmenite were obtained with a Cameca SXFive Field Emission EPMA instrument, equipped with five WDS spectrometers, and housed at the Microscopy and Microanalysis Unit (MMU), University of the Witwatersrand, Johannesburg. Operating conditions were: 15 kV accelerating potential, 20 nA beam current, <1 μm spot diameter, and counting times of 20 and 10 s on peaks and backgrounds, respectively. For Cr-Fe-Ti oxide minerals, corrections were made for the overlap of the TiK_β and VK_α X-ray peaks by subtracting a percentage of V counts determined empirically by measuring V on a V-free standard (TiO_2 or Ti metal). Morgan and London (1996) reported that analysis of hydrous, alkali, aluminosilicate glasses like ours, at the operating conditions we used, can result in Na-loss of up to 10%. However, most of our glasses have <3 wt. % Na_2O (Figure 6e), and even if the results for Na are underestimated, it

Table 1
Whole Rock Major and Trace Element Compositions of Karoo Picrites

												Average		Average	
	KS-35a	KP-97		KP-108		KP-111		KP-142		KP-144		Karoo picrite		Lesotho basalt	
Data source[a]	1	1	2	1	2	1	2	1	2	1	2	$n = 897$		$n = 579$	
Latitude	−23.1686	−22.6111		−22.4944		−22.4819		−22.3511		−22.3817					
Longitude	31.5053	31.2222		31.2014		31.2192		31.1247		31.2142		Avg	Std dev	Avg	Std dev
SiO_2	49.96	48.65	46.59	47.20	45.70	49.26	47.24	50.27	49.84	49.16	49.48	48.42	1.71	50.19	0.91
TiO_2	2.68	3.19	2.73	2.51	2.16	3.17	2.97	3.84	3.39	3.17	2.87	2.33	0.82	1.00	0.13
Al_2O_3	9.95	7.01	6.00	6.54	5.61	8.00	7.28	8.46	7.50	8.10	7.29	9.04	1.79	14.95	0.77
FeO^T			11.73		11.13		10.31		10.80		11.13				
$Fe_2O_3^T$	12.52	11.59		11.59		10.60		10.99		10.60					
FeO[b]	10.14	9.39	10.55	9.39	10.02	8.58	9.27	8.90	9.72	8.58	10.02	9.38	0.91	8.63	0.81
Fe_2O_3[b]	1.25	1.16	1.30	1.16	1.24	1.06	1.15	1.10	1.20	1.06	1.24	1.84	0.18	1.69	0.16
MnO	0.17	0.14	0.15	0.14	0.15	0.14	0.14	0.14	0.14	0.13	0.15	0.16	0.03	0.18	0.02
MgO	11.30	16.44	20.72	20.52	24.17	13.92	15.75	12.53	14.45	14.53	18.17	15.39	3.24	6.86	1.24
CaO	8.63	6.22	5.10	5.62	4.57	6.71	5.99	7.00	6.01	6.40	5.46	7.43	1.33	10.33	0.70
Na_2O	1.92	0.27	0.27	1.98	1.55	1.51	1.47	1.16	1.09	1.31	1.16	1.46	0.47	2.13	0.36
K_2O	1.67	4.02	3.14	0.97	0.79	2.47	2.02	3.05	2.55	2.69	2.28	1.30	0.86	0.67	0.35
P_2O_5	0.40	0.53	0.45	0.46	0.37	0.55	0.52	0.57	0.51	0.48	0.42	0.35	0.15	0.17	0.03
H_2O^+	1.77	1.91	n.d.	3.29	n.d.	3.14	n.d.	3.22	n.d.	2.12	n.d.	0.00			
H_2O^-	0.39	0.45	n.d.	0.33	n.d.	0.81	n.d.	0.55	n.d.	0.55	n.d.	0.00			
LOI	2.16	2.36	2.99	3.62	3.67	3.95	6.20	3.77	3.60	2.67	1.46	2.91	1.42	3.19	1.41
Total	100.23	99.38	100.00	100.11	100.00	99.32	100.00	100.79	100.00	98.28	100.00	100.00		100.00	
mg#[e]	66.51	75.73	77.77	79.57	81.13	74.30	75.16	71.50	72.60	75.11	76.37	74.04	3.90	58.37	4.49
$Na_2O + K_2O$	3.59	4.29	3.41	2.95	2.34	3.98	3.49	4.21	3.64	4.00	3.44	2.84	0.91	2.88	0.64
ppm															
Cs			0.51		0.69		2.34		1.12		0.74	0.95	0.76		
Rb	36	82	67.7	67	52.3	101	85.6	56	46.7	53	45	29.92	19.81	14.51	17.22
Ba	667	840	665	1,076	841	1,154	1,110	1,295	1,194	1,320	1,096	603.86	373.98	206.72	53.23
Th			3.5		4.07		6.07		5.58		6.23	3.86	2.10		
U			0.34		0.9		1.23		1.01		1.27	2.41	2.34		
Nb		19.8	18.73	21.9	18.92	27.1	24.34	27.9	14.83	34	21.77	17.55	9.25	7.19	2.89
Ta			1.3		1.7		2.3		2.4		2.6	0.92	0.80		
La			38.4		48.1		71.4		90.2		69.3	35.34	20.68	11.68	3.06
Ce			95.7		109.9		148.1		177.5		154.4	77.46	44.89	26.89	4.80
Pb			n.d.		n.d.		8		8		7	5.49	4.69		
Pr			12.25		13.15		19.54		23.12		18.78	9.25	6.66		
Sr	826	870	820	956	834	1,168	1,102	1,536	1,304	1,417	1220	697.19	345.34	191.25	42.21
Nd			56.4		54.8		79.5		91.8		75.1	47.37	24.86	14.62	8.04
Sm			9.78		9.59		14.2		16.23		12.5	7.75	4.57	3.86	0.77
Zr	302	415	307	390	281	451	404	547	453	474	385	266.53	130.75	96.85	17.78
Hf			7.9		7.4		10.8		12.1		9.8	5.27	3.80		
Eu			2.73		2.43		3.84		4.42		3.27	2.31	1.15		
Gd			7.36		6.69		9.71		11.43		8.79	6.62	3.16	23.33	7.09

Table 1
Continued

	KS-35a	KP-97		KP-108		KP-111		KP-142		KP-144		Average Karoo picrite		Average Lesotho basalt	
Data source[a]	1	1	2	1	2	1	2	1	2	1	2	$n = 897$		$n = 579$	
Latitude	−23.1686	−22.6111		−22.4944		−22.4819		−22.3511		−22.3817					
Longitude	31.5053	31.2222		31.2014		31.2192		31.1247		31.2142		Avg	Std dev	Avg	Std dev
Tb			0.93		0.78		1.08		1.16		1.02	0.96	0.35	3.77	1.58
Dy			4.59		3.97		5.84		6.56		5.07	5.23	1.64	18.10	11.76
Y	29.4	26.5	19.4	22.6	15.6	27	24.1	31.6	26	27.5	21	25.10	5.60	26.70	3.85
Ho			0.79		0.75		1		1.1		0.83	0.93	0.31	3.36	2.36
Er			1.87		1.64		2.24		2.42		2.00	2.24	0.67	6.29	2.81
Tm			0.25		0.26		0.34		0.35		0.29	0.39	0.42	0.81	0.34
Yb			1.32		1.24		1.62		1.6		1.47	1.73	0.97	5.45	3.39
Lu			0.22		0.19		0.28		0.24		0.22	0.23	0.07	0.52	0.10
Be			1.5		1.3		1.7		1.8		1.8				
Sc	26.6	21	16.4	16.3	14.6	20.1	18.6	22.5	19.3	18.9	16.5	21.39	4.98	33.72	3.74
V	246	200	186	155	152	201	208	215	219	180	173	214.66	113.74	252.84	31.04
Cr	636	858	932	861	824	792	862	699	949	700	826	912.88	305.36	254.26	104.53
Co	69	77	88.8	105	95.4	66	65.8	64	71.2	70	78.7	75.40	13.34	44.73	5.77
Ni	495	920	1,179	1,306	1,491	709	816	618	737	779	936	723.37	252.06	84.50	43.76
Cu	88	84	76	74	83	91	100	93	98	84	81	79.61	22.50	98.82	23.92
Zn	110	110	124	106	106	99	98	109	105	99	101	105.43	12.44	89.87	9.54
Mo			1		1.1		1.1		0.8		1.2	1.54	1.15		
Ga			12.3		11.7		16.1		16.5		13.7	14.50	3.74		
Sn			4		4		5		5		4	4.30	1.53		
Li			5		10		14		9		10		0.03		

[a]Data Sources: 1. Bristow (1984) and Bristow et al. (1984). 2. Kamenetsky et al. (2017). [b]Calculated with FeO = 90% FeO^T. [c]$H_2O^+ + H_2O^-$. [d]Calculated by difference from 100%. [e]$100Mg/(Mg + Fe^{2+})$.

would have minimal effect upon the relationships and interpretations we discuss below. EPMA data are given in Table S1. Back-scattered electron (BSE) images and X-ray intensity maps were acquired using the same operating conditions as for quantitative elemental analyses. BSE images were obtained using 30 s frame times, and X-ray maps for individual elements were acquired using 750–1,500 points, typically at 2-μm intervals, with dwell times of 10 ms per point.

H_2O and CO_2 concentrations in glasses from the Karoo picrites were determined using the virtual Secondary Ion Mass Spectrometry (SIMS) facility at the University of the Witwatersrand, which is connected via an internet-based link to the Cameca 1280-HR instrument located at the GeoForschungsZentrum Potsdam, Germany. Four samples were prepared by extracting areas of interest from thin sections and casting these discs in Epofix epoxy using 1-in. diameter polycarbonate rings (with an 18 mm inside diameter), so as to minimize outgassing. A total of three such mounts were made, containing a total of nine areas of interest. An additional mount containing seven basaltic reference glasses (Shishkina et al., 2010) with independently determined H_2O contents was used for our SIMS calibration. Four of these reference glasses had also been previously characterized for their CO_2 contents, allowing us to determine both H_2O and CO_2 contents concurrently. Our SIMS analyses took place over the course of a single three-day period, during which we conducted a total of 28 determinations on the reference samples along with 31 determinations on the Karoo samples. The results from these glasses appear in Table S2. The average pressure in the sample chamber was 6.4×10^{-7} pascals, consistent with only modest sample outgassing. The relative sensitivity factors (RSF) for

Table 2
Petrographically Estimated Modal Abundances of Karoo Picrites

	KS-35A	KP-97	KP-108	KP-111	KP-142	KP-144
Phenocrysts (%)	10	23	37	20	20	20
Olivine	94	82	90	89.1	64.2	89.1
Altered olivine	5	17.5	9	9.9	15.8	9.9
Clinopyroxene					19	
Cr-rich spinel	1	0.5	1	1	1	1
	100	100	100	100	100	100
Groundmass (%)	90	77	63	80	80	80
Glass, Type 1	35	48.2		33.1	55	
Glass, Type 2		5.3	56.4	17.9		
Feldspar	39					49
Clinopyroxene	20	36.7	34.4	39.2	33.3	40
Ilmenite	5	5.6	3.9	4.4	8.5	10
Mt-rich spinel		3.3	4.4	4.4	1.8	
Apatite	1	0.9	0.9	1	1.4	1
	100	100	100	100	100	100
Overall mode						
Olivine	9.4	18.9	33.3	17.8	12.8	17.8
Altered Olivine	0.5	4.0	3.3	2.0	3.2	2.0
Glass, Type 1	31.5	37.1		26.5	44.0	0.0
Glass, Type 2		4.1	35.5	14.3		
Feldspar	35.1	0.0	0.0	0.0	0.0	39.2
Clinopyroxene	18	28.3	21.7	31.4	32.6	32.0
Ilmenite	4.5	4.3	2.5	3.5	5.0	8.0
Mt-rich spinel		2.5	2.8	3.5	1.1	
Cr-rich spinel	0.1	0.1	0.4	0.2	0.2	0.2
Apatite	0.9	0.7	0.6	0.8	1.1	0.8
	100	100	100	100	100	100
Mean olivine core Fo	83.8 ± 2.1	83.8 ± 1.0	84.5 ± 3.6	87.1 ± 2.3	83.3 ± 0.5	82.0 ± 1.1
Number of analyses	20	25	21	24	47	9
Olivine rims						
Min Fo	65.1	72.0	65.8	61.9	serp*	77.7
Max Fo	79.5	81.9	82.5	86.4	serp*	79.3
Number of analyses	22	10	15	17		4

serp* rims obliterated by serpentine alteration.

hydrogen and carbon were determined from the measured $^{16}O^{1}H^{-}/^{30}Si^{-}$ and $^{12}C^{-}/^{30}Si^{-}$ ratios, respectively. We found a very strong linear correlation ($R^2 = 0.985$) between $[H_2O/SiO_2]_{true}$ vs. $[^{16}O^{1}H^{-}/^{30}Si^{-}]_{SIMS}$; the equation of this best-fit line was used to quantify the H_2O wt. % contents in the "unknown" Karoo samples. We estimate our data quality to be around ±12% Relative Standard Deviation (RSD) based on the repeatability of $n = 6$ determinations on the M49 reference glass, which has an assigned H_2O content of 1.25 wt. %. In contrast, the results from the CO_2 portion of our experiment were more equivocal. The RSF, as defined by the measured $^{12}C^{-}/^{30}Si^{-}$, dropped by a factor of nearly seven over the 43-h period of data acquisition. Hence,

the data we were able to recover for CO_2 can only be considered semiquantitative. Details about our SIMS data acquisition and data reduction are given in Table S2.

Trace element concentrations of selected phases were acquired by LA-ICPMS at the Earthlab, University of the Witwatersrand, employing an Australian Scientific Instruments (ASI) Resonetics Resolution 193 nm ArF excimer (SE 155) system coupled to a Thermo Scientific Fisher sector-field ICPMS (Element XR). Measurements were performed in low resolution and electrostatic scanning (E-scan) modes. Data were acquired by single spot analysis (diameter = 30–40 μm), using a laser repetition rate of 8 Hz and a fluence of 2.5 J cm^{-2}. Total signal acquisition time was 65 s to allow for data processing and preparation for the next analysis, comprising 15 s of preablation and postablation (gas blank) and 30 s of ablation measurements. Laser sampling took place in an SE155 dual-volume ablation cell (Laurin Technic, Canberra, Australia) using a mixed He-Ar atmosphere and a small volume of N_2 to enhance signal stability and sensitivity. The following gas flows were applied: He (300–400 ml/min), Ar (800–1,000 ml/min), and N_2 (3–5 ml/min). Synthetic glass NIST 612 (Jochum et al., 2011) served for calibration, while NIST 610 and 614 as well as USGS natural glasses BHVO2, BCR-2, and BIR-2 (Gao et al., 2002) were analyzed as unknowns to evaluate accuracy and precision. The LA-ICPMS system was tuned during line scans using NIST 612 glass for maximum sensitivity for ^{6}Li, ^{115}In, and ^{238}U, while maintaining oxide levels (ThO^{+}/Th) < 0.2%. For internal standardization, the isotopes ^{43}Ca or ^{29}Si were used. Typically, two analyses of the primary calibration standard were obtained at the beginning and end of an experiment, and 10–20 analyses of unknowns were followed by analyses of one primary calibration standard and two to four analyses of the secondary standards for quality control purposes. Prior to each spot analysis surface material was removed using two laser pulses. The following masses were measured: ^{29}Si, ^{43}Ca, ^{45}Sc, ^{47}Ti, ^{51}V, ^{53}Cr, ^{59}Co, ^{60}Ni, ^{65}Cu, ^{85}Rb, ^{88}Sr, ^{89}Y, ^{90}Zr, ^{93}Nb, ^{139}La, ^{140}Ce, ^{141}Pr, ^{146}Nd, ^{147}Sm, ^{151}Eu, ^{157}Gd, ^{159}Tb, ^{163}Dy, ^{165}Ho, ^{166}Er, ^{169}Tm, ^{174}Yb, ^{175}Lu, ^{178}Hf, ^{181}Ta, ^{208}Pb, ^{232}Th, ^{238}U. All isotopes were measured in triple mode, including pulse counting, analog and Faraday cup, depending on signal. Data reduction was performed using the iolite extension (http://www.iolite.org.au) to the software Igor Pro (http://www.wavemetrics.com), specifically the data reduction scheme ("DRS") "X_Trace_Elements_IS," proceeding in a series of sequential steps, including data import, selection of integrations, baseline subtraction, drift and down-hole fractionation, calibration and error propagation (Paton et al., 2010, 2011).

4. Results

4.1. Petrography

Petrographically estimated modal abundances of our samples are given in Table 2. Most consist of 10–30% euhedral to subhedral olivine phenocrysts and glomerocrysts (0.5–2 mm across), set in a fine-grained groundmass of glasses and mineral phases (Figures 3 and S1–S5); glass is absent in sample KP-144. Vesicles and amygdales are absent in all studied samples. Olivine phenocrysts in all samples contain 0.5–1% of small (10–300 μm), rounded, equant inclusions of Cr-rich spinel, and lesser amounts of partly crystallized, rounded melt inclusions (up to 100 μm across), similar to those described by Kamenetsky et al. (2017). The olivines have been variably serpentinized (5–18%) along irregular fractures and phenocryst rims up to 250 μm across. One sample (KP-142) contains 4% of euhedral to subhedral clinopyroxene microphenocrysts up to 200 μm across, in addition to 16% olivine phenocrysts.

The groundmass in most samples contains abundant (17–56%), irregular patches up to 4 mm across of unaltered, light to dark brown glass. Two samples, KP-97 and KP-111, have the unusual feature of containing two compositionally distinct glasses, which are distinguishable optically, in BSE images (Figures 4, 5, 7, and 9) and in X-ray maps. The dominant glass in the groundmass of these samples (65–90% of total glass) is lighter brown in color, has a lighter gray BSE response, and is designated as Type 1 glass. The darker brown glass, with darker gray BSE color, is lesser in volume (9–35% of total glass), mainly occurs adjacent to olivine phenocrysts, and is designated as Type 2 glass. Boundaries between the two glasses are sharp, but irregular, as shown in BSE images (Figures 4, 5, 7, and 9). The principal groundmass minerals are clinopyroxene (20–40%), which occurs as equant to irregular to acicular grains up to 400-μm long, ilmenite (4–10%) needles and skeletal grains up to 200-μm long, and equant grains of Fe-rich spinel (1–4%) up to 100 μm across. Accessory apatite occurs as small equant grains and stubby needles up to 1–1.5-μm long. Two samples contain

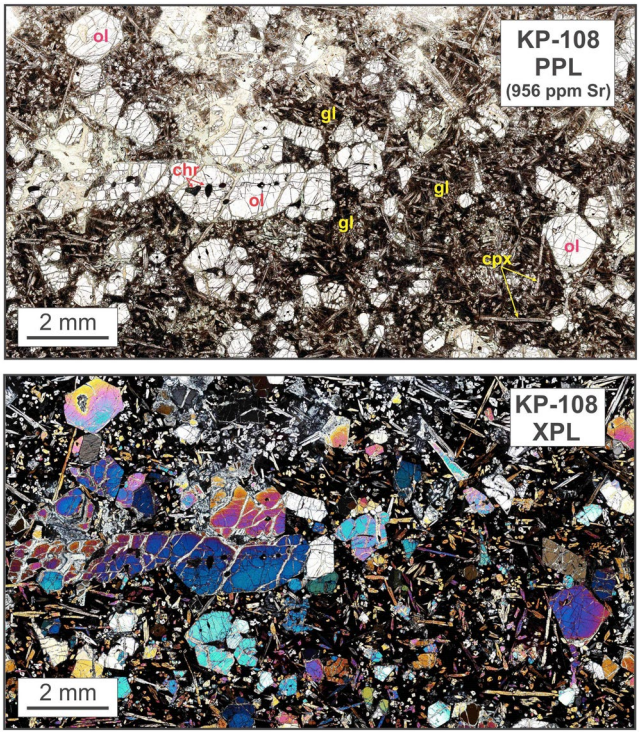

Figure 3. Full thin section photomicrographs of Sr-rich (956 ppm) picrite sample KP-108 in plane-polarized (top) and crossed-polarized (bottom) light, showing the textures and mineralogy typical of the studied samples. Olivine (ol) phenocrysts up to 2 mm across contain inclusions of Cr-rich spinel (chr), and the groundmass is composed of acicular clinopyroxene (cpx), dark brown glass (gl), ilmenite needles, and apatite grains (both too small to be resolved at this scale). Full thin section photomicrographs of the other five picrite samples in this study are pictured in Figures S1–S5.

groundmass feldspars. Those in KS-35A (39% of groundmass) occur as subhedral laths up to 400-μm long, commonly with lamellar twinning; some grains show hollow, skeletal crystal forms. The laths are interstitial to larger clinopyroxene grains, and are closely associated with irregular patches of brown glass. Feldspars in KP-144 (49% of groundmass) occur as aggregates of untwined, stubby laths up to 150-μm long, and irregular, anhedral grains. In some cases, the laths form clusters of curved or bent crystals; less common are acicular needles up to 250-μm long. Patchy compositional zoning of KP-144 feldspars is evident in BSE images, which reveal irregular patches in the central regions of grains that have a darker BSE response, surrounded by brighter areas at the outer portions of grains. Orthopyroxene, while present in some Karoo picrites (Bristow, 1980, 1984), is absent in our samples, and secondary alteration products are completely absent in all groundmass phases.

4.2. Electron Microprobe Analyses

4.2.1. Olivine

Olivine phenocryst compositions are relatively homogeneous except for very thin rims (20–30-μm wide) that show continuous normal zoning to more Fe-rich compositions (Figure 5). Average core compositions range from $Fo_{82.02 \pm 1.1}$ in sample KP-144 to $Fo_{87.1 \pm 2.3}$ in sample KP-111 (Fo = molar Mg/[Mg + Fe]), with maximum variability of 3.6 mole % Fo (Figure S6 and Table 2). Fe-rich rims range down to $Fo_{61.9}$ in sample KP-111, although serpentinization along phenocryst rims has variably obliterated the Fe-rich crystal edges; sample KP-142 has especially thick serpentine rims (up to ~250 μm) that have totally replaced the Fe-rich zoned phenocryst margins. Analyses of serpentine in KP-142 are given in Table S1. Ni and Cr concentrations in olivine correlate positively with Fo (cores up to 0.63 wt. % NiO, and 0.42 wt. % Cr_2O_3; rims down to 0.12 wt. % NiO, and 0.01 wt. % Cr_2O_3, Figure S7). Mn and Ti correlate negatively with Fo (cores down to 0.08 wt. % MnO, and 0.01 wt. % TiO_2; rims up to 0.51 wt. % MnO, and 0.12 wt. % TiO_2) (Figure S7). We do not see the

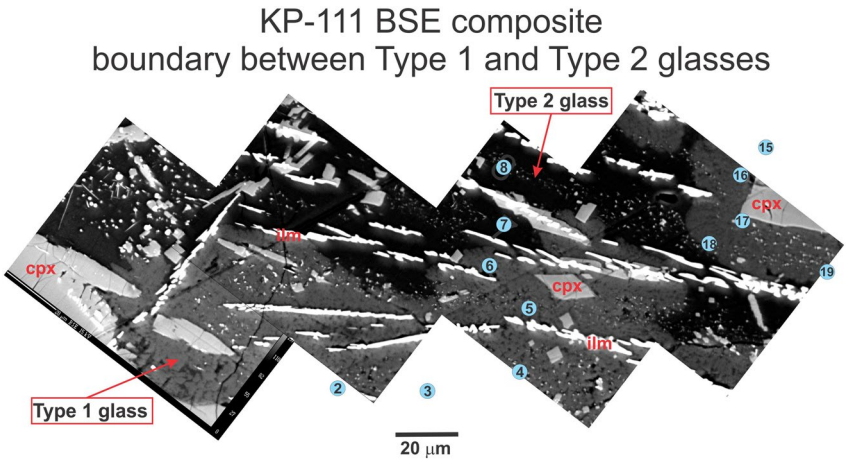

Figure 4. Composite BSE image of groundmass in sample KP-111 showing the sharp, but irregular boundary between Type 1 and Type 2 glasses. Type 2 glass (darker gray) has higher Na_2O, CaO, and H_2O, and lower K_2O, FeO, MgO, and Mg# relative to Type 1 glass (lighter gray). Locations of EPMA analyses of glasses (Table S1) are shown as blue circles. Equant to irregular clinopyroxene (cpx) and needles of ilmenite (ilm) are labeled in red. Note that the abundant, but volumetrically minor tiny mineral grains in both glasses, rendering spot analyses of pure glasses challenging.

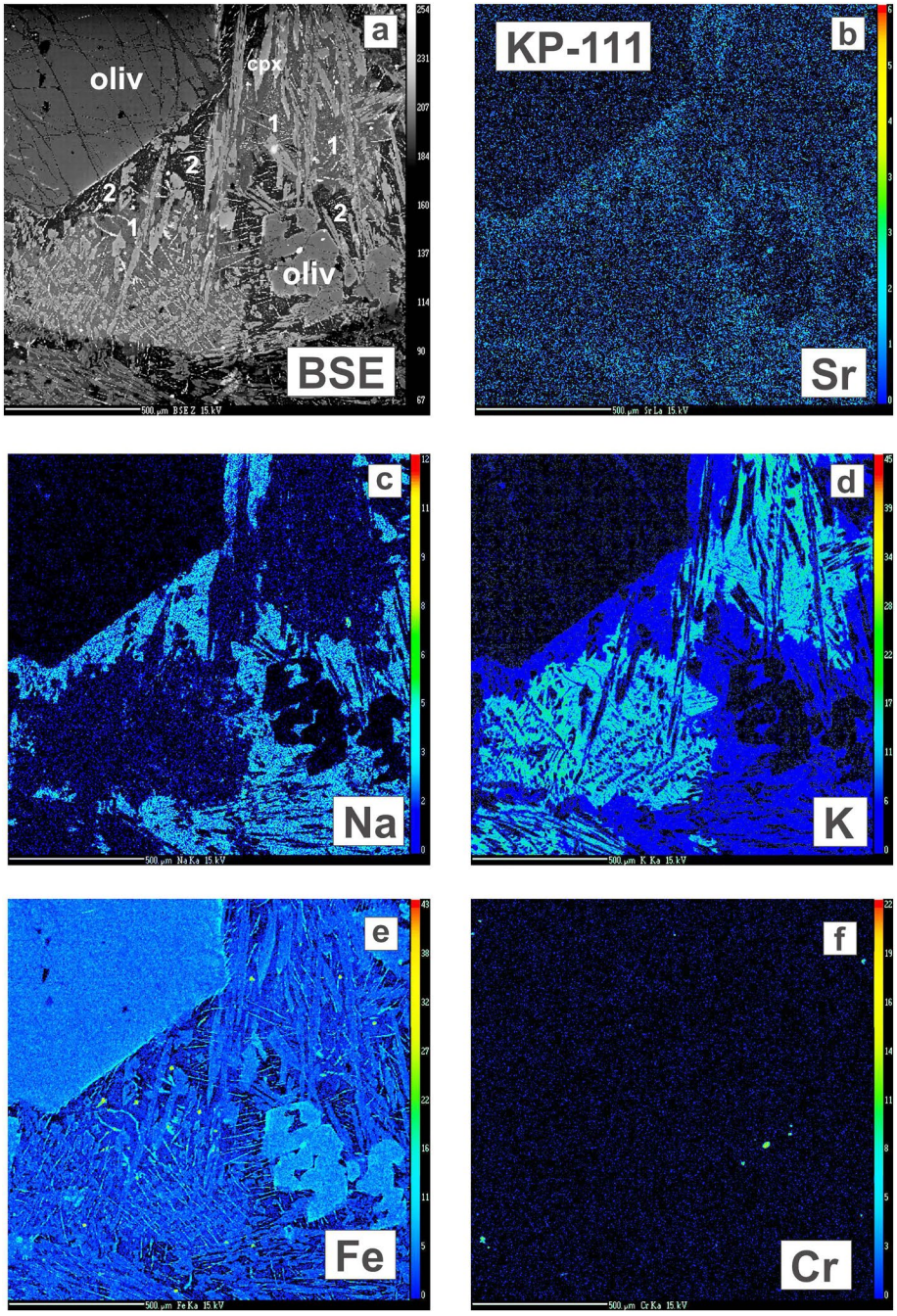

Figure 5. Back-scattered electron (BSE) image (a) for a part of picrite sample KP-111 and X-ray maps for Sr (b), Na (c), K (d), Fe (e), and Cr (f). This sample contains 20% olivine phenocrysts and a groundmass with 51% glass (Types 1 and 2), 40% clinopyroxene, 4% ilmenite needles, 4% Fe-rich spinel, and 1% apatite (Table 2). Type 1 glass (medium gray in (a) and labeled as "1") is dominant in the groundmass and contains lower Sr (b), lower Na (c), lower Fe (d) and higher K (d) relative to Type 2 glass (dark gray in (a) and labeled as "2"), which occurs adjacent to olivine phenocrysts. Note the thin Fe-rich rims at the edges of olivine phenocrysts, as seen in (e). The X-ray map for Cr (f) shows the locations of Cr-rich spinel grains; as in Figures 8 and 9, the high counts for Sr in Cr-rich spinel (b) are caused by an overlap of the Sr L_α X-ray peak (which was used for imaging) with a third-order Cr K_α peak, reflecting Cr, rather than Sr concentration. Scale bar at the bottom of each image is 500-μm long.

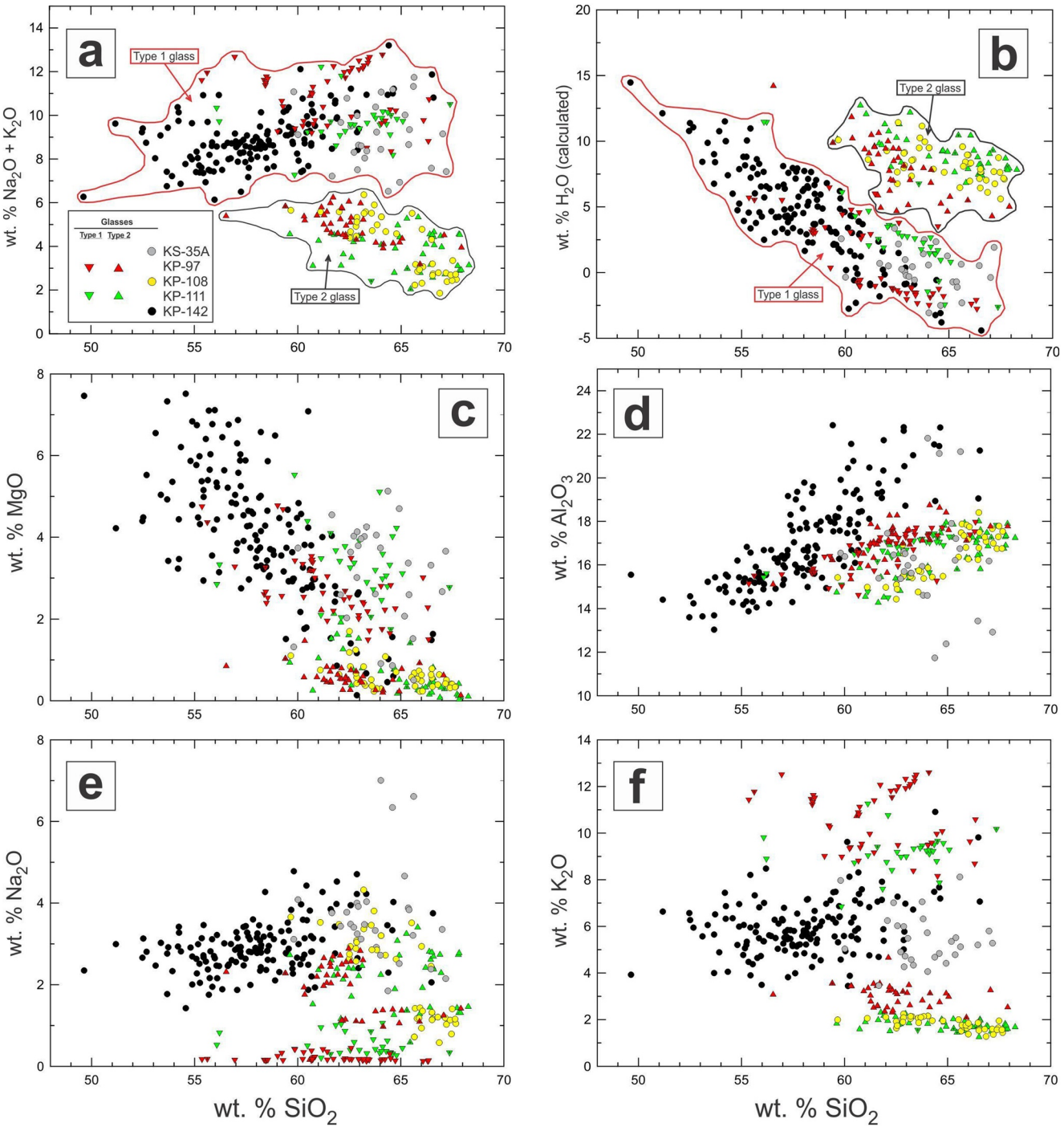

Figure 6. (a) Compositions of glasses in the studied picrite samples as determined by EPMA on plots of wt. % SiO_2 vs. (a) total alkalies (TAS diagram, fields for different lithologies are given in Figure 1), (b) wt. % H_2O (calculated as difference from EPMA summation totals), (c) MgO, (d) Al_2O_3, (e) Na_2O, and (f) K_2O. Two groupings are apparent, with one group having higher Na_2O + K_2O, MgO, Al_2O3, Na_2O, and K_2O, and lower calculated H_2O (includes glasses in samples KS-35A, KP-142 and Type 1 glasses in KP-97 and KP-111). A second group with lower Na_2O + K_2O, MgO, Al_2O3, Na_2O, and K_2O, and higher calculated H_2O includes glasses in KP-108 and Type 2 glasses in KP-97 and KP-111). Spot analyses clearly representing mixtures of glasses with incorporated mineral inclusions are omitted.

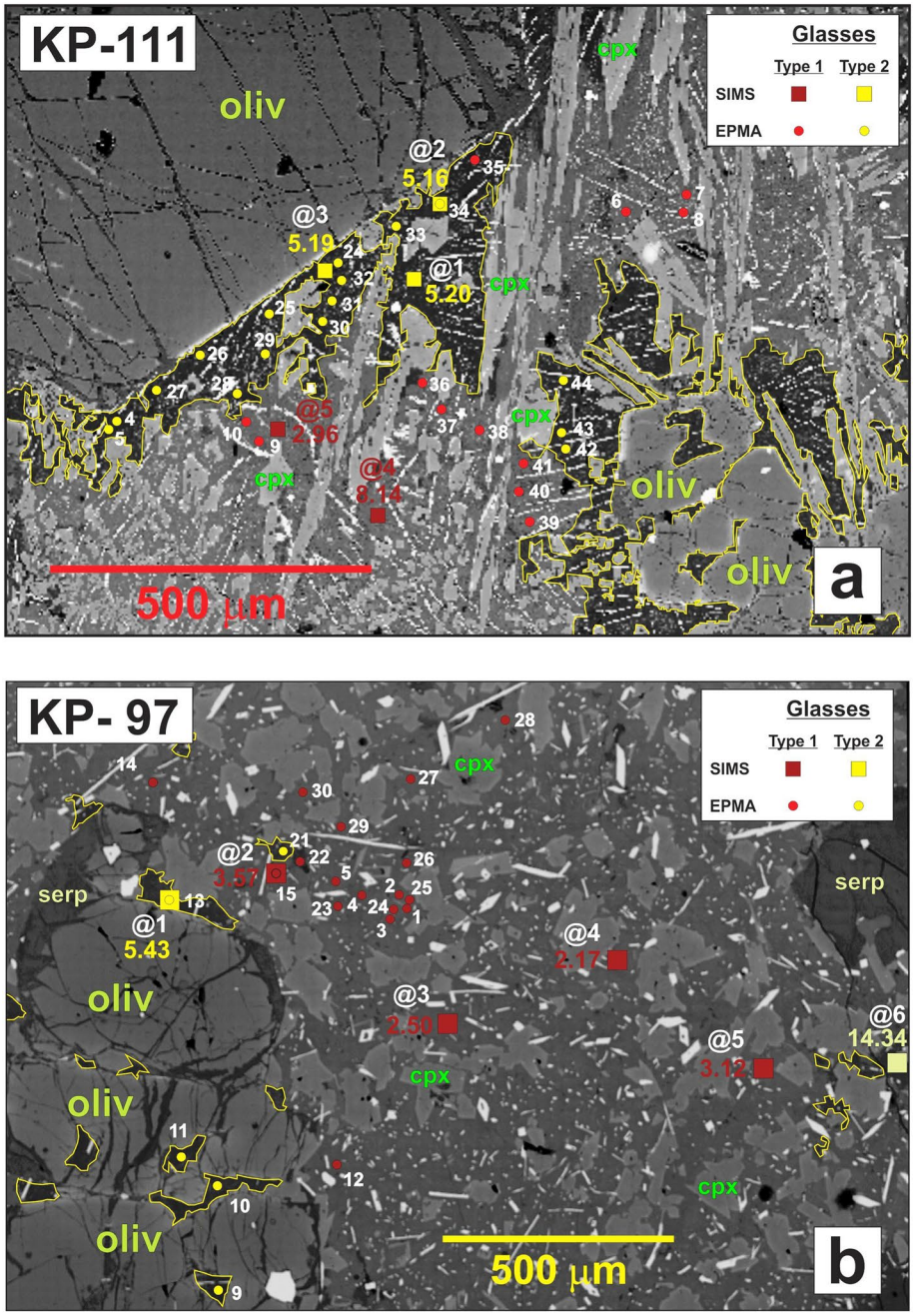

Figure 7. BSE images of parts of (a) KP-111 and (b) KP-97, showing the results of SIMS measurements of H_2O in Type 1 (red symbols) and Type 2 (yellow symbols) glasses. Spot locations are indicated in white for SIMS analyses (squares) and EPMA analyses (circles), and are keyed to individual analyses given in Tables S2 and S1, respectively. Type 2 glasses that occur adjacent to olivine phenocrysts (oliv) have dark gray BSE response, and are outlined in yellow. Type 1 glasses, which dominate the groundmasses, have a lighter gray BSE response. Numbers in red or yellow represent wt. % H_2O as measured by SIMS for Type 1 and Type 2 glasses, respectively. Type 2 glasses have higher measured average H_2O (KP-97: $H_2O = 3.66 \pm 0.10$ wt. %, $n = 5$; KP-111: $H_2O = 3.59 \pm 0.04$ wt. %, $n = 3$) relative to Type 1 glasses (KP-97: $H_2O = 1.45 \pm 0.69$ wt. %, $n = 6$; KP-111: $H_2O = 2.84 \pm 0.86$ wt. %, $n = 6$). Images (a) and (b) may be compared with BSE images and X-ray element maps given in Figures 5 and 9, respectively. Averages exclude spots with admixed serpentine (e.g., KP-111@4).

correlations between Fo and Ca that were reported in Karoo picritic olivines by Kamenetsky et al. (2017); CaO in the olivines we analyzed ranges from 0.15 to 0.41 wt. % CaO. Likewise, no correlations are apparent between Fo and Al, Zn, Na, or K.

4.2.2. Clinopyroxene

All clinopyroxenes are compositionally zoned, showing Mg-rich and Ca-poor cores that vary continuously to more Fe-rich and Ca-rich regions toward grain edges (Figure S6 and Table S1). The most primitive clinopyroxenes are the microphenocrysts in KP-142, which have cores of $Wo_{35.6–38.6}$, $En_{55.2–53.6}$, zoned to rims of $Wo_{41.8}$, $En_{42.8}$. Pyroxenes occurring as equant to acicular groundmass phases tend to be slightly less primitive, and have more evolved grain edges, up to $Wo_{47.9–48.7}$, $En_{28.4–30.5}$ (Figure S6). Compositional profiles show strong positive correlations of Mg# (= molar Mg/[Mg + Fe]) with Cr_2O_3 and NiO, and negative correlations with Al_2O_3, TiO_2, MnO, Na_2O, and K_2O, such that the Mg-rich cores of phenocrysts and grains have low Al_2O_3 (~1 wt. %, Figure S8a), TiO_2 (~1 wt. %), MnO (~0.1–0.15 wt. %), Na_2O (0.2–0.25 wt. %), and K_2O (<0.05 wt. %), and high Cr_2O_3 (0.9–1.0 wt. %, Figure S8b) and NiO (0.12 wt. %). Grain edges and rims have very high Al_2O_3 (to 7–8 wt. %, Figure S8a) and TiO_2 (to 4.2–4.9 wt. %), moderately high MnO (to 0.3 wt. %), Na_2O (to 0.6–0.7 wt. %), and K_2O (to 0.2 wt. %), and low Cr_2O_3 (<0.02 wt. %, Figure S8b) and NiO (<0.01 wt. %).

4.2.3. Spinels

The highly variable compositions of spinels (Figure S9 and Table S1) correlate with their textural associations. Grains entirely enclosed within olivine phenocrysts have higher Cr_2O_3 and MgO relative to those at host phenocryst edges or within the groundmass, which are enriched in TiO_2, FeO, and Fe_2O_3. Overall, the spinel compositions form a trend from early Cr-rich and Mg-rich chromites toward Ti-rich magnetites that corresponds to the "Fe-Ti trend" of Barnes and Roeder (2001), and the "spinel gap" they describe is evident in our data set. These features are illustrated in a triangular plot of molar Fe^{3+}-Cr-Al (Figure S9). The most evolved spinels are Ti-rich magnetites with TiO_2 = 11.3–19.5 wt. % that occur as equant groundmass phases in sample KP-111. In sample KP-144, spinel grains that protrude into the groundmass from within olivine phenocrysts show continuous zoning from Cr-rich interiors toward Fe-rich and Ti-rich compositions in the outer regions, as illustrated in X-ray element maps (Figure S10). Similar features were described by Barnes and Kunilov (2000) for picrites from the Noril'sk and Talnakh intrusions of Siberia and by Scowen et al. (1991) for porphyritic olivine basalts in the Kilauea Iki lava lake, Hawaii, and were interpreted as reflecting reaction of Cr-rich spinels with evolving, trapped residual liquids.

4.2.4. Ilmenite

Ilmenite needles in picrite groundmasses vary in composition, most notably in TiO_2 and MgO, which correlate positively from TiO_2 ~ 42 wt. % and MgO ~ 0.6 wt. % to TiO_2 ~ 51 wt. % and MgO ~ 5 wt. % (Figure S11 and Table S1). There is also a weak correlation of TiO_2 with Cr_2O_3, but other elements show no significant correlations. The highest MgO and TiO_2 ilmenites in samples KP-97 and KP-144 approach the compositions of picroilmenites commonly found in kimberlites (Wyatt et al., 2004). Similar results for ilmenites in Karoo picritic rocks were reported by Cawthorn et al. (1989).

4.2.5. Feldspars

Feldspar compositions in KS-35A and KP-144 (Table S1) are shown on an Ab-An-Or diagram in Figure S12. Subhedral feldspars in KS-35A are plagioclases that show an overall range from about $An_{51–52}Or_{3–5}$ to $An_{23–25}Or_{8–15}$ (average = $An_{42.2 \pm 8.2}Or_{5.9 \pm 3.1}$). Individual laths show restricted compositions that typically vary by <3–4 mole % An and Or; compositional zoning features are very minor to absent. In KP-144, the irregular, more centrally located patches with darker BSE response are enriched in plagioclase components, forming a cluster that ranges in composition from about $An_{15–19}Or_{21–23}$ to $An_{34–35}Or_{4–12}$. The outer regions of grains, with lighter BSE response, form a K-rich compositional array from about $An_{11–12}Or_{37–39}$ to $An_{2–3}Or_{80–81}$. There is a slight tendency for the most Or-rich compositions to occur near the outer rims of grains, but no systematic compositional zoning patterns are apparent. Feldspars from both samples have average TiO_2 = 0.18 ± 0.09 wt. % and FeO = 0.81 ± 0.43 wt. % (n = 85) (Table S1). Feldspars and glasses in sam-

ples KS-35A and KP-144 plot between the 800 and 1,000 °C solvus isotherms of Elkins and Grove (1990) (Figure S12).

4.2.6. Glasses

Microprobe analyses of glasses are not straightforward because they contain variable amounts of tiny mineral inclusions (mainly clinopyroxene, ilmenite, and apatite), which are not always visible optically or even in high-resolution BSE images. However, it is possible to recognize the chemical effects of incorporated mineral inclusions in individual spot analyses by abnormally high concentrations of MgO and CaO (for clinopyroxene inclusions), TiO_2 and FeO (for ilmenite), or P_2O_5 and CaO (for apatite), and in some cases, the presence of multiple mineral inclusions can be identified in a similar way. A tabulation of individual glass analyses and averages that excludes (or minimize) mineral inclusions ($n = 307$) are given in Table S1; spot analyses representing various mixtures of glass, clinopyroxene and ilmenite, and/or apatite inclusions ($n = 73$) are highlighted and are excluded from the averages. It is possible that we have underestimated, to some extent, the number of glass analyses "contaminated" by mineral inclusions.

Most glasses are very rich in alkalies (~2–13 wt. % $Na_2O + K_2O$), and two compositional groups can be distinguished on a TAS diagram (Figure 6a). One group, with $Na_2O + K_2O = 6.3–13.2$ wt. % and $SiO_2 = 50–67$ wt. %, includes glasses from KS-35A, KP-142 (Type 1), and Type 1 glasses in KP-97 and KP-111, and ranges in composition from basaltic trachyandesite to trachyte. A second group, including glasses from KP-108 and Type 2 glasses in KP-97 and KP-111, has $Na_2O + K_2O = 1.9–6.4$ wt. % and $SiO_2 = 55–68$ wt. %, and ranges from andesite to dacite (Figure 6a). These groupings are maintained for some elements (Figures 6b–6f), but glasses from individual samples form distinct fields that overlap to varying degrees. Sample KP-142 contains the most compositionally variable glasses; those from some other samples form variably diffuse linear arrays on oxide-oxide plots (Figure 6). There is almost complete compositional overlap of fields for some elements like CaO and P_2O_5. The best chemical discriminators for the various types of glasses are the alkalies; fields for SiO_2 vs. Na_2O or K_2O show the most distinct separation (Figures 6e and 6f). Additional plots of glass compositions are given in Figures 10–14 and S13–S18.

For samples KP-97 and KP-111, Type 1 glasses, the dominant groundmass phase, have markedly higher K_2O (8.2–12.6 wt. %) and lower Na_2O (0.13–0.45 wt. %) relative to Type 2 glasses ($K_2O = 2.1–4.7$, $Na_2O = 1.8–2.9$ wt. %), which occur adjacent to olivine phenocrysts. This is readily apparent in X-ray maps for K and Na (Figure 5). Type 1 glasses are also relatively enriched in MgO, FeO, and MnO, depleted in TiO_2 and CaO, but show almost complete overlap for SiO_2, Al_2O_3, and P_2O_5.

4.3. Secondary Ion Mass Spectrometry (SIMS) Analyses

SIMS analyses were carried out in order to measure the H_2O and CO_2 concentrations in the glasses. The results (Table S2) demonstrate that the volatile budget of the glasses is dominated by H_2O, with negligible CO_2 (maximum = 1,291 μg/g), which is consistent with the absence of deuteric carbonate phases. For samples with two glasses, it is apparent that Type 2 glasses, adjacent to olivine phenocrysts have higher H_2O (3.64 ± 0.09 wt. %, $n = 8$) than Type 1 glasses in the groundmasses (2.15 ± 1.04 wt. %, $n = 12$). This is illustrated on BSE images of samples KP-111 and KP-97, on which the locations of analysis spots are given (Figure 7). Type 2 glasses in KP-108 have $H_2O = 3.36 \pm 0.93$ wt. % ($n = 5$), and Type 1 glasses in KP-142 have $H_2O = 1.22 \pm 0.80$ wt. % ($n = 4$). Averages exclude spots with admixed serpentine (e.g., KP-111@4, Table S2).

The high H_2O content of the glasses in our samples can also be assessed, albeit more imprecisely, by examining the EPMA summation totals, which are highly variable between and within different samples. H_2O contents, calculated by difference from EPMA totals, are given in Table S1 and plotted in Figure 6b. Although H_2O contents calculated by difference are imprecise, possibly because of element losses (e.g., Na, as discussed above) at the high beam currents used for analysis, comparison of the results with H_2O values determined by SIMS shows that the EMPA data maintain some of the important relationships, if only in a relative sense; this includes the higher H_2O content of Type 2 glasses relative to those of Type 1 glasses. We also consider as approximately correct that the H_2O content of glasses show similar groupings to those evi-

dent for SiO_2 vs. $Na_2O + K_2O$ (Figures 6a and 6b), and the negative correlation of H_2O and SiO_2, especially for sample KP-142 (Figure 6b).

4.4. X-ray Maps and BSE Images

We obtained BSE images and X-ray element maps of our Karoo picrite samples in order to identify the repository phase(s) for the high incompatible trace element concentrations revealed by the whole rock data. Viable possibilities include glass, feldspar, apatite, secondary alteration products like serpentine, and possibly clinopyroxene. We chose to investigate the distribution of Sr as an indicator of incompatible trace element enrichment. Figure 8 shows a BSE image and X-ray maps for P, Ti, and Sr in sample KP-144, which contains 20% olivine phenocrysts and a groundmass consisting of 49% feldspar, 40% clinopyroxene, 10% ilmenite, and 1% apatite; glass is absent from this sample (Table 2). The X-ray map for P (Figure 8b) shows that apatite occurs as equant and elongate grains up to 20 μm across, and ilmenite occurs as abundant needles and blocky grains up to 500 μm across, as shown by the Ti X-ray map (Figure 8c). The X-ray map for Sr (Figure 8d) reveals that apatite, ilmenite, olivine, and serpentinized olivine are virtually devoid of Sr, and that clinopyroxene may contain minor Sr concentrations. Rather, the main repository for Sr in this sample appears to be the groundmass feldspar. Note that the high apparent X-ray response for Sr in Cr-rich spinel is caused by an overlap of the Sr L_α X-ray peak (used for imaging) with a third-order Cr K_α peak, and reflects Cr, rather than Sr concentration (Figures 5, 8d, and 8b).

Images for sample KP-97 (30% olivine phenocrysts, groundmass composed of 63% Type 1 and Type 2 glasses, 30% clinopyroxene, 6% ilmenite and 1% apatite) are shown in Figure 9. The X-ray map for Sr (Figure 9b) clearly shows that the glasses are the main repository of Sr, with Type 2 glass, which occurs adjacent to olivine phenocrysts, having much higher concentrations than Type 1 glass, which is the dominant phase in the groundmass of this sample. Clinopyroxene grains in the groundmass show modest X-ray signals for Sr. Quantification of the trace element concentrations of glasses and other phases is discussed in the next section.

4.5. LA-ICPMS Analyses

Using LA-ICPMS analysis, we targeted glasses and feldspars, and to a lesser extent pyroxenes, in order to identify and characterize the repositories of incompatible elements in our samples. Given the relatively large spot sizes (30–40 μm), trace element compositions of glasses are quite variable because of the unavoidability of incorporating variable amounts of mineral contaminants, either at grain boundaries, as small inclusions or as concealed subglass mineral grains. This problem is diminished for EPMA measurements because of the smaller spot size used (<1 μm). Mineral contaminants include olivine, clinopyroxene, ilmenite, and to a lesser extent apatite, whose presence is indicated by EMPA analyses for major elements. The effect of the presence of these mineral contaminants on the LA-ICPMS spot analyses is to lower the concentrations of incompatible elements, and so those results with the highest values of Sr, Ba, Zr, REE, etc. will most closely reflect the compositions of pure glasses.

LA-ICPMS results for trace elements in glasses, feldspars, and clinopyroxenes are given in Table S1, and are plotted for Sr, Ba, and Zr in Figure 10. Plots for major and trace elements of glasses and mineral phases in individual samples are given in Figures S13–S18. Average glass compositions (Table S1) are plotted on a primitive mantle-normalized spider diagram in Figure 11a. In feldspar-free samples KP-108 and KP-142, glasses least affected by mineral contamination have Sr ~ 3,000–3,400 ppm, Ba ~ 3,000–3,300 ppm, Zr ~ 1,000–1,200 ppm, and Ce ~ 400–450 ppm. For samples that contain two glass types (KP-97, KP-111), the dominant groundmass glass (Type 1) has markedly lower Sr (600–1,800 ppm) than glass adjacent to olivine phenocrysts (Type 2), which has Sr ~ 2,700–9,500 ppm, but other incompatible elements are highly variable, providing no clear cut distinction between glasses of Types 1 and 2 (Ba ~ 300–5,000 ppm, Zr ~ 200–1,100 ppm, Ce ~ 100–400 ppm). Sample KS-35A contains both glass and feldspar as groundmass phases, but the few LA-ICPMS spot analyses we obtained for these phases show lower incompatible element concentrations than the whole rock values, implying that additional data are needed to more accurately locate the repositories of these elements in this sample. Besides glass, clinopyroxene is the only other

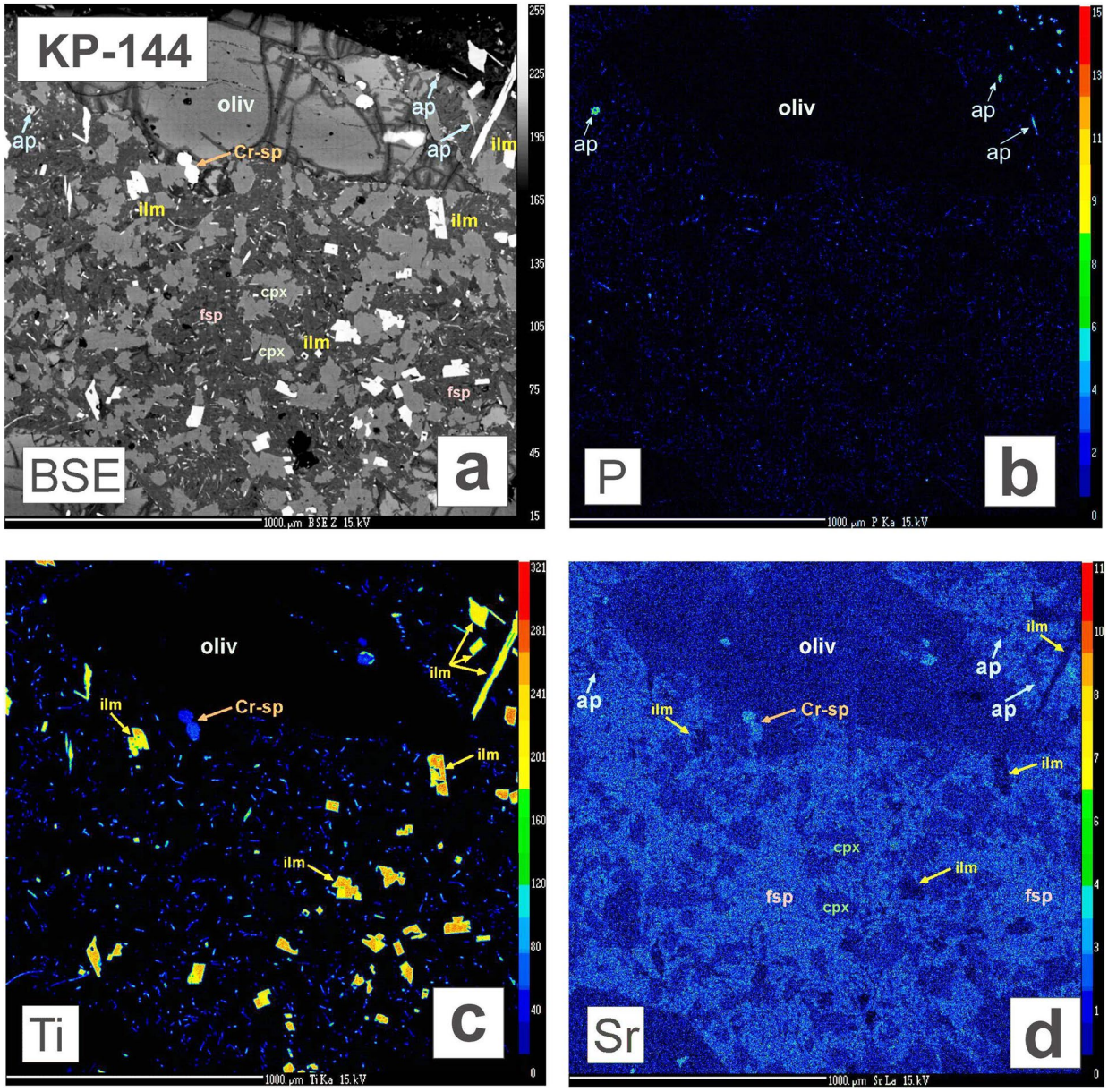

Figure 8. Back-scattered electron (BSE) image (a) for a part of picrite sample KP-144 and X-ray maps for P (b), Ti (c), and Sr (d). This sample contains 20% olivine phenocrysts and a groundmass with 49% feldspar, 40% clinopyroxene, 10% ilmenite needles, and 1% apatite. Glass is absent. The X-ray image at bottom right shows that Sr is concentrated in feldspar, and to a far lesser extent, in clinopyroxene, but is absent from all other phases. Note that the high counts for Sr in Cr-rich spinel are caused by an overlap between the Sr L_α X-ray peak (which was used for imaging) with a third-order Cr K_α peak, and reflects Cr, rather than Sr concentration.

phase that contains appreciable Sr (~130–580 ppm), as measured in samples KP-97, KP-111, and KP-142 (Figure 10). A single spot analysis of olivine in sample KP-111 yields very low concentrations (<5–6 ppm) for all measured trace elements.

Chondrite-normalized (values from Anders and Grevesse (1989)) REE plots are shown in Figure 12. Glasses have relatively high REE abundance levels, with La_N = 33–470, which in most cases are higher than their whole rock values: KP-97, La_N (chondrite-normalized La concentration) = 45–307, WR = 86; KP-108, La_N = 120–450, WR = 108; KP-111, La_N = 95–450, WR = 160; KP-142, La_N = 140–470, WR = 202. Sample KP-142, for which we have the most LA-ICPMS glass analyses (n = 98), shows this effect nicely: there are a large number of subparallel REE patterns, almost all of which plot above the whole rock pattern (Figure 12).

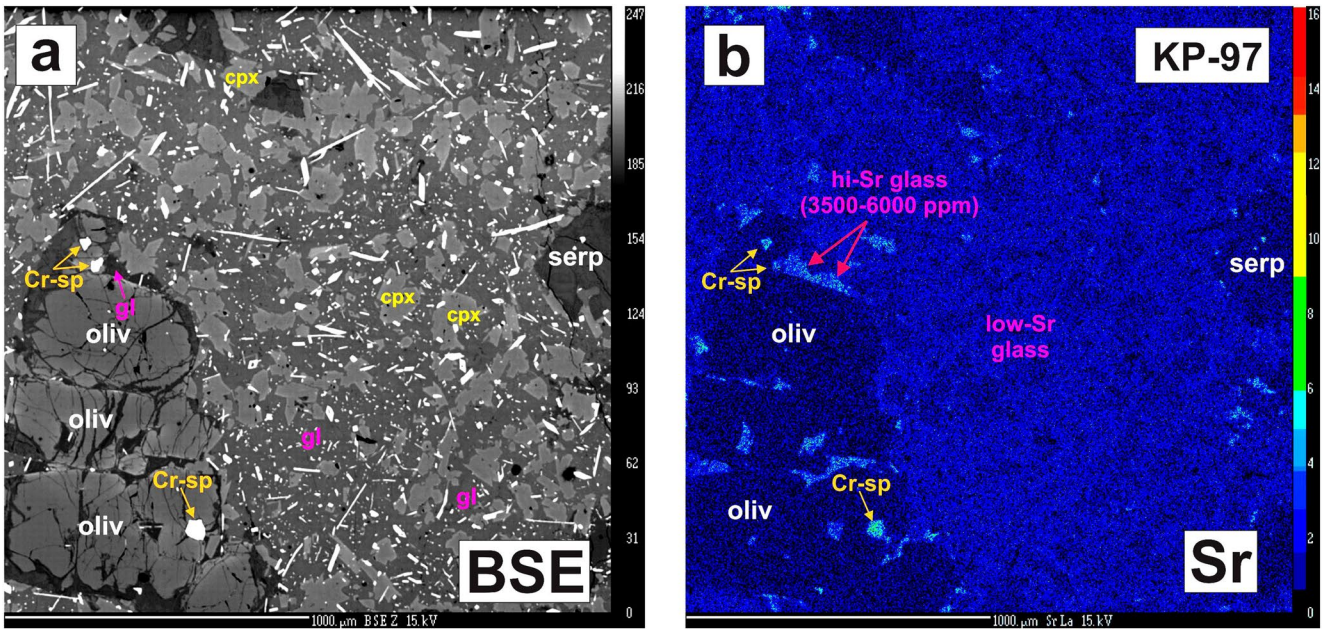

Figure 9. BSE image (a) and X-ray map for Sr (b) in part of sample KP-97, which contains two compositionally distinct glasses (gl). The dominant glass in the groundmass (Type 1, medium gray in BSE image) contains lower Sr (207–1,860 ppm) relative to Type 2 glass, which occurs adjacent to olivine (oliv) phenocrysts (Sr = 920–9,470 ppm, dark gray in BSE image). Serpentinized olivine (serp) has similar BSE response to Type 2 glass. Clinopyroxene (cpx) grains in the groundmass show modest X-ray signals for Sr. As in Figures 5b and 8d, the high apparent Sr response for Cr-rich spinel (Cr-Sp) is caused by an overlap between Sr and Cr X-ray peaks.

Glass analyses with REE lower than whole rock values tend to be those affected by incorporation of mineral inclusions. Glasses are typically LREE-enriched, with $[La/Lu]_N$ ranging from ~20 to ~28; where present, Eu anomalies (expressed as Eu/Eu* = Eu_N/(SmN × GdN) tend to be negative (Eu/Eu* = 0.69–0.96), although some small positive Eu anomalies with Eu/Eu* ~ 1.1 are also present; the majority of glass analyses show no Eu anomalies. There is near complete overlap of REE patterns for Type 1 and Type 2 glasses in samples KP-97 and KP-111. Sample KS-35A contains coexisting feldspar and glass, with most feldspars showing low REE abundance levels (La_N = 1.5–4.3) and prominent positive Eu anomalies (Eu/Eu* = 1.5–22.7), and most glasses showing higher total REE (La_N = 30–175) and small negative Eu anomalies (Eu/Eu* = 0.63–0.74). Spot analyses of clinopyroxenes are characterized by LREE depletion, at variable abundance levels; those in KP-97 and KP-142 have La_N = 3–33, whereas those in KP-111 has La_N = 68–177. A single analysis of olivine in KP-111 has low REE abundances, with La_N = 1.7 and Lu_N = 0.14.

5. Discussion

5.1. Mass-Balance Calculations: Constraints on Parental Melt Compositions

Based on our petrographic observations and whole rock and mineral geochemistry, the picrites we studied can be interpreted as mixtures of variably accumulated phenocrysts and evolved interstitial melts represented by bulk groundmass compositions. We computed bulk groundmass compositions for each sample by subtracting from whole rock compositions the mean phenocryst compositions measured by EPMA and LA-ICPMS (olivine, early Cr-rich spinel and clinopyroxene in KP-142) in their modal proportions (Table 2). Results of these calculations are given in Table S3. Whole rock compositions were normalized to 100 wt. % after recalculating FeO as 90% of FeO_{total}, excluding H_2O^-, and assuming that H_2O^+ or LOI represents magmatic water contained in glasses and hydrous mineral phases like apatite. Mean mineral compositions were also normalized to 100 wt. %. Two interpretations for the physical and chemical evolution of the picrites are offered below, representing closed-system and open-system petrogenetic models. In the closed-system model, the calculated bulk groundmass compositions represent the evolved residual liquids in equilibrium with the phenocrysts; for the open-system model, bulk groundmasses represent infiltration of unrelated

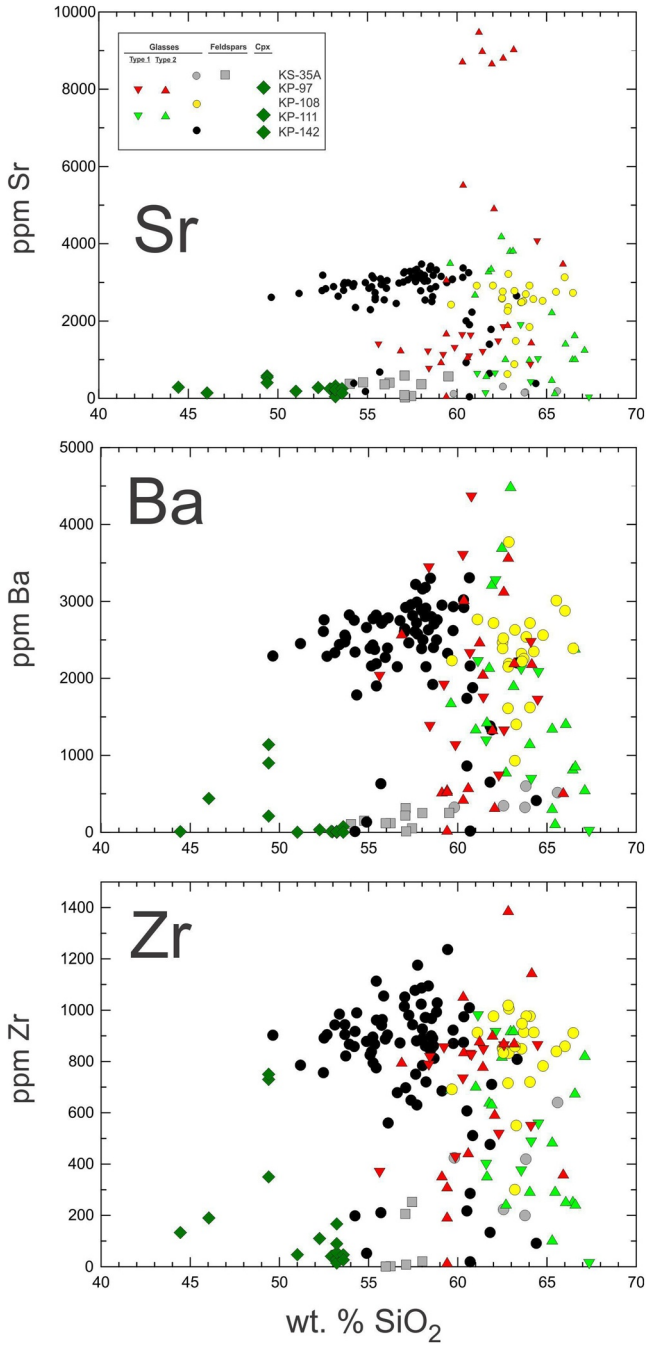

Figure 10. Plots of wt. % SiO_2 vs. Sr, Ba, and Zr showing compositions of glasses in the studied picrite samples, as determined by LA-ICPMS and EPMA. Spot analyses clearly representing mixtures of glasses with incorporated mineral inclusions are omitted.

melts into an accumulation of earlier-formed olivine phenocrysts, with or without surrounding intercumulus melt formed by olivine fractionation (Figure 13).

In either model, Type 1 glasses in the picrites can be assumed to represent the last phases to form in the groundmasses, after quench crystallization of clinopyroxene, ilmenite, late Fe-rich spinel apatite and feldspar, if present. Liquid evolution paths can be calculated by subtracting bulk groundmass minerals, in proportions given by modal abundances, from bulk groundmass compositions as determined above. Again, mean groundmass mineral compositions were normalized to 100 wt. %. In most cases, the liquid evolution trajectories for major and trace elements correspond to measured glass compositions, especially those determined to be minimally affected by mineral inclusion contamination (Figures 14 and S13–S18). For samples with two glasses, the liquid evolution trajectories trend toward the Type 1 glass (KP-97, Figure S14) or toward a composition between Types 1 and 2 glasses (KP-111, Figure S16). These calculated liquid evolution trajectories may be compared with liquid lines of descent as determined using thermodynamically constrained fractional crystallization modeling, discussed below.

For models of closed-system evolution, the picrites represent variable mixtures of accumulated phenocrysts and evolved residual liquids, and in this case, the compositions of their parental liquids must lie between whole rock and bulk groundmass compositions. We estimated parental liquids as mixtures of 50% each of whole rock and bulk groundmass compositions; varying these proportions makes little difference because the maximum difference between the end-members, e.g., in SiO_2, is less than about 2 wt. %. Estimated parental liquid compositions for three samples (KS-35A, KP-111, and KP-142) have Mg#s in equilibrium with measured olivine compositions, using the K_d values for Fe^{2+}-Mg partitioning between olivine and melt determined by Ulmer (1989). Parental liquids for the other three samples (KP-97, KP-108, KP-144) have Mg#s higher than equilibrium values, implying compositions with excess olivine. For these samples, we adjusted the compositions by subtracting 1% increments of equilibrium olivine and recalculated the compositions of olivine and liquid, repeating this until liquid and olivine achieved equilibrium Mg#s. This required 7% subtraction of olivine for samples KP-97 and KP-144, and 11% olivine subtraction for KP-108. Calculations can be found in Table S3, and a summary of parental melt compositions for major and trace elements is given in Table 3. Parental melt compositions are used below for liquid evolution modeling. Average calculated parental melts have basalt-like SiO_2 (50.8 ± 0.5 wt. %), but lower Al_2O_3 (9.5 ± 0.6 wt. %) and Na_2O (1.6 ± 0.8 wt. %), higher MgO (9.3 ± 0.5 wt. %), and much higher K_2O (2.9 ± 1.3 wt. %) relative to the average Lesotho tholeiite (Table 3). Most trace elements, including all incompatible elements (avg. Sr = 1,290 ± 329 ppm, Ba = 1,217 ± 314 ppm, Zr = 493 ± 98 ppm) and even some compatible elements (avg. Ni = 520 ± 152 ppm, Cr = 551 ± 214 ppm, Co = 87 ± 25 ppm) are much higher than those of average Lesotho tholeiite. For open-system models, compositions of infiltrating (Type 1) melts can be calculated as bulk groundmasses minus the modal proportions of Type 2 glasses, if present (Figure 13). Calculations of these melt compositions are given in Table 3. Note that the compositions of parental melts to the intercumulus melts surrounding olivine phenocrysts prior to infiltration of Type 1 melts cannot be precisely constrained because the amount of prior olivine fractionation is not

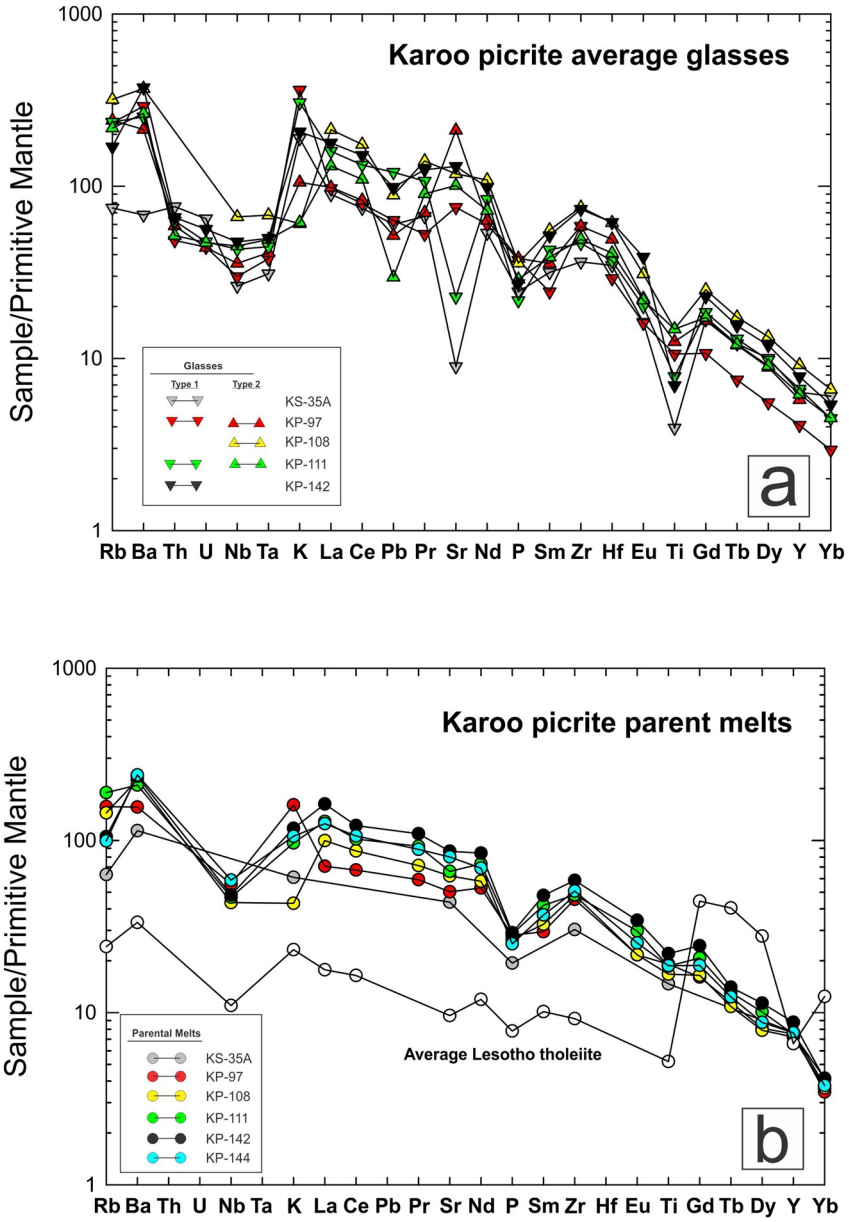

Figure 11. Primitive mantle-normalized spider diagrams of trace elements in (a) average glasses (Table S1) and (b) calculated parent melts of the studied picrites (Table 3). Primitive mantle values are from White (2020).

known. However, these parental melts must lie between the compositions of olivine and Type 2 glasses, and are illustrated in Figure 13 as a range of possible compositions with ~50 wt. % SiO_2.

5.2. Fractional Crystallization Modeling

For closed-system evolution, we explored the details of fractional crystallization processes to account for the observed mineral and glass compositions in the Karoo picrites, using the PELE (version 8.01b) modeling software (Boudreau, 1999), which is a PC platform of MELTS (Ghiorso & Sack, 1995). We used parental liquids as determined above (Table 3) to calculate isobaric fractionation models for individual picrite samples. Input parameters were as follows: P = 5 kbar, fO_2 = QFM, excluded phases = orthopyroxene (absent in our samples), apatite (to suppress early crystallization of phosphate), and spinel (to prevent excessive early crystallization of Cr-rich spinel). The pressure of 5 kbar was chosen as a value between the expected depths

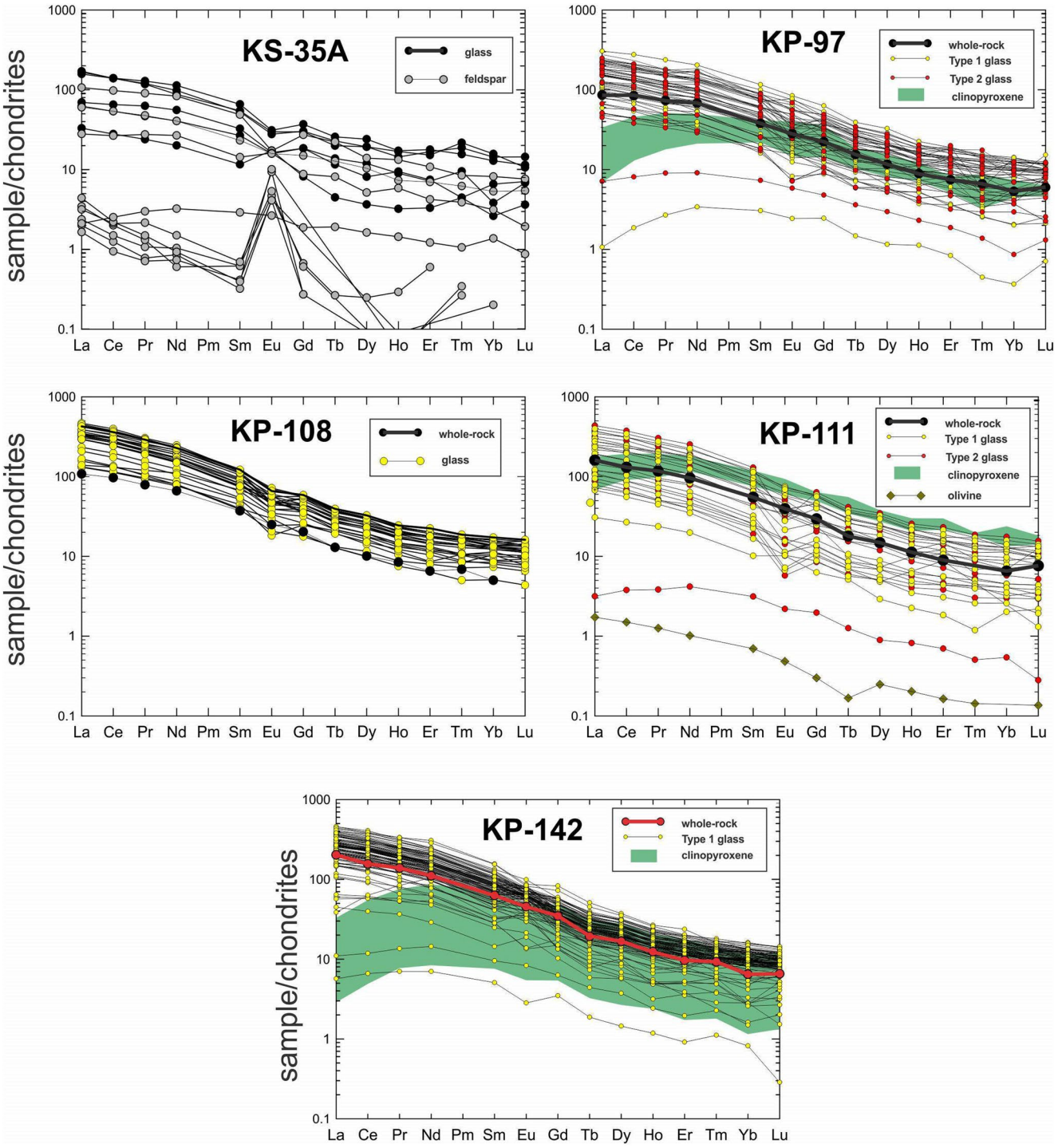

Figure 12. Chondrite-normalized (Anders & Grevesse, 1989) REE plots of glasses and minerals in the studied picrite samples. Obvious mixtures of glass and mineral inclusions have been omitted, but patterns for some glasses that plot below whole rock values may represent mixtures of glass and tiny mineral inclusions.

of initial and final crystallization, but varying P in the range of 0–10 kbar has minimal effect on the results for liquid and solid evolution. Likewise, varying fO_2 between QFM + 1 and QFM − 1 has minimal effect on the calculations. Results are given in Table S4 and plotted for SiO_2 vs. MgO and Sr in sample KP-142 in Figure 14; plots for a variety of major and trace elements in the other five samples are given in Figures S13–S18.

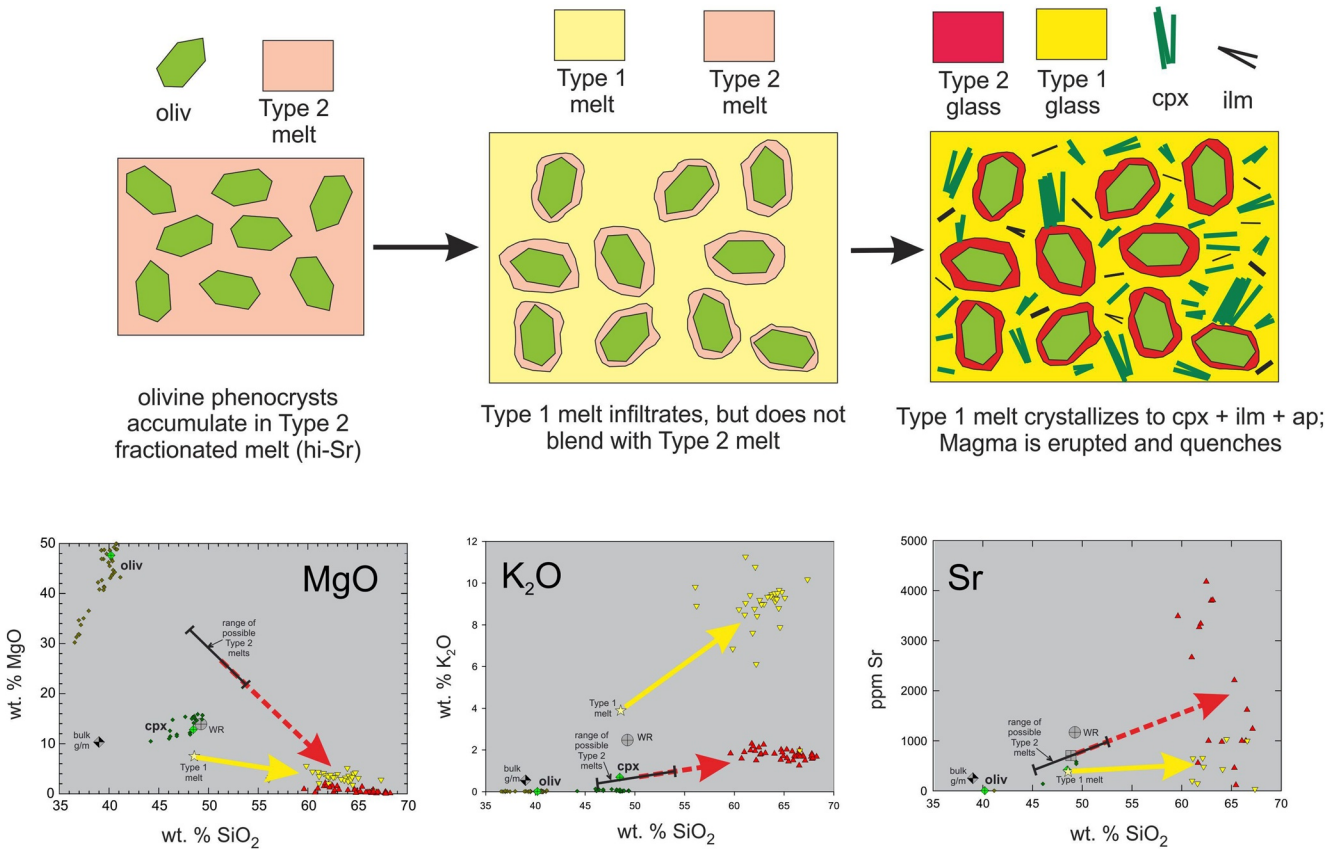

Figure 13. Top panel shows schematic diagrams illustrating open-system petrogenetic model based on sample K-111, which contains two distinct glasses. An accumulation of olivine phenocrysts surrounded by Sr-rich Type 2 melt formed by extensive fractional crystallization (left) is infiltrated by, but does not blend with, genetically unrelated Type 1 melt (center). Upon eruption (right), Type 2 melt quenches to Type 2 glass around olivine phenocrysts, and Type 1 melt quench crystallizes to clinopyroxene + ilmenite + apatite, and residual Type 1 melt quenches to Type 1 glass. Bottom panel shows plots of wt. % SiO_2 vs. MgO, K_2O, and Sr, illustrating liquid evolution paths for Type 2 melt by olivine removal (red arrows) and Type 1 melt by quench crystallization of bulk groundmass minerals (yellow arrows). Note that the compositions of Type 2 melts cannot be constrained precisely because the amount of prior olivine fractionation is not known, and are shown as a range of possible compositions.

The crystallization sequences are: olivine − clinopyroxene ± Fe-rich spinel ± ilmenite − feldspar. Clinopyroxene joins olivine after about 12–30% crystallization, and late feldspar precipitates after about 50–70% crystallization, although most picrites quenched to form glass before the onset of feldspar crystallization. For most samples, the liquidus olivine compositions predicted by PELE are within a few mole % Fo of the average core olivine compositions measured by EPMA, but differ by ~6 mole % Fo for samples KP-108 and KP-144, perhaps due to underestimation of FeO/Fe_2O_3 in their parental liquids.

For most major and trace elements, the PELE liquid evolution models closely follow those predicted independently by the bulk groundmass and mineral calculations described above, and the calculated liquids just before feldspar crystallization best match the measured compositions of those glasses deemed to have minimal contamination by mineral phases (Figures 14 and S13–S18). For feldspar-bearing samples, PELE modeled liquids either evolve to major element compositions near average measured feldspar (KP-144) or to between coexisting feldspar and glass (KS-35A); regrettably, insufficient trace element analyses have been acquired for glasses and feldspars in these samples. In general, the correspondence of PELE models with crystallization sequences and phase composition confirms the veracity of parental liquid compositions, the origins of which are discussed below.

For open-system evolution, in which the compositions of infiltrating melts (Type 1 melts, Table 3) are represented by bulk groundmasses (or by bulk groundmasses minus minor Type 2 glasses), crystallization, and subtraction of bulk groundmass phases from infiltrating melts yields evolved liquids that closely match

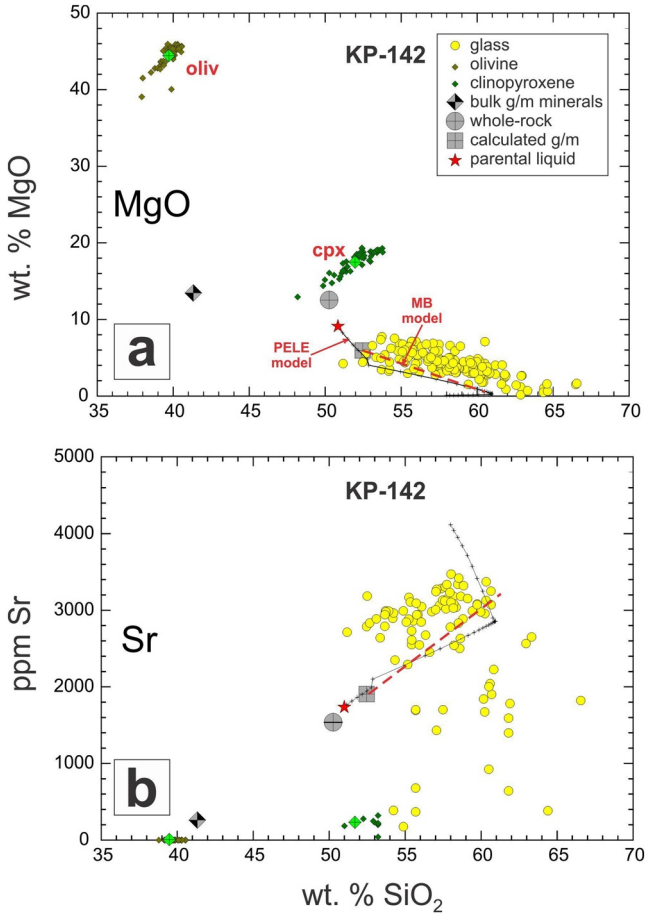

Figure 14. Plots of wt. % SiO_2 vs. MgO (a) and ppm Sr (b), showing compositions of glasses, olivines (oliv), and clinopyroxenes (cpx). Average mineral compositions are shown as large green diamonds. Also shown are compositions of whole rocks (gray crossed circles), bulk groundmass minerals calculated from modal abundances (gray crossed diamonds), bulk groundmasses (g/m) calculated by subtracting bulk groundmass minerals from whole rocks (gray crossed squares), and calculated parental liquids (red stars). The results of fractional crystallization modeling using PELE are shown as black lines with + symbols at temperature intervals of 25 °C. The inflection point at 61 wt. % SiO_2 represents the feldspar-in step; note that melts in most samples quenched before this point was reached. PELE models may be compared with a simple mass balance (MB) liquid line of descent (dashed red lines) calculated by subtracting compositions of bulk groundmass minerals from that of bulk groundmasses.

Type 1 glasses (Figure 13). Likewise, evolved liquids modeled using PELE approach Type 1 glasses after crystallization of clinopyroxene, ilmenite, and Fe-rich spinel. Fractionation of olivine from the parents to Type 2 melts (which can only be approximated, as stated above) results in liquid evolution paths that approach the compositions of Type 2 glasses (Figure 13).

5.3. Closed-System vs. Open-System Petrogenesis

For closed-system magmatic evolution, we interpret the compositional differences between Type 2 glasses, which occur as small patches adjacent to olivine phenocrysts in samples KP-97 and KP-111, relative to the dominant (Type 1) glass in the groundmasses, as reflecting additional growth of Fe-rich olivine that occurs as thin rims along phenocryst edges. This resulted in removal of olivine components (e.g., MgO, FeO) from the Type 1 melts, and dramatic enrichment in nonolivine components (Na_2O up to ~3.4 wt. %, H_2O to 3.6 wt. %, and Sr to ~9,000 ppm) observed in the compositionally distinct Type 2 glasses (Figures 6, 7, and 10). It is difficult to evaluate this effect for other incompatible elements (e.g., Ba, Zr, REE) because of the extensive overlap for Types 1 and 2 glasses, probably caused by unavoidable incorporation of mineral contaminants in the spot analyses. We are puzzled by the lack of enrichment in K_2O for Type 2 glasses (Figure 13); no K-rich phases (e.g., K-feldspar) occur in the groundmasses of these samples. Secondary removal of K from the Type 2 glasses is a possibility, but this seems unlikely, given the absence of low-temperature secondary phases such as zeolites or clay minerals.

Some of these perceived problems are obviated for an open-system model whereby olivine phenocrysts accumulated in a fractionated, high-Sr magma, now represented by the thin Type 2 glass rims observed in samples KP-97 and KP-111. This crystal-rich slurry was then infiltrated by a compositionally distinct melt, whose composition can be calculated as bulk groundmass minus the modal proportion of high-Sr Type 2 glass. The two melts cannot have blended, because the boundaries between Types 1 and 2 glasses are sharp, but irregular (Figures 4, 5, 7, and 9). The open-system model accounts for the problem with the lack of K_2O enrichment in Type 2 glasses, as mentioned above (compare Figures 13 and S16).

If the blended system erupted immediately after infiltration by Type 1 melt, then Type 2 melt surrounding olivine would have been quenched to Type 2 glass, and Type 1 melt would quench crystallize to clinopyroxene, ilmenite, Fe-rich spinel, and apatite, with residual melt forming the abundant Type 1 glass in the groundmass. The mechanics of this open-system model are illustrated in Figure 13, which also shows the fractionation effects on chemical plots of SiO_2 vs. MgO, K_2O, and Sr. This illustration is based on sample KP-111, which has relatively abundant Type 2 glass (overall 14 modal %, Table 2) and dominant Type 1 glass (overall 27 modal %), but could also be applied to the other sample with two glasses (KP-97), which has a much lower amount of Type 2 glass (4 modal %). In this case, the preinfiltrated mush would have had a larger proportion of accumulated olivine crystals, resulting in lesser Type 2 glass surrounding the phenocrysts. Samples with only a single glass might be explained if they formed by infiltration of an almost pure olivine cumulate, with vanishingly small amounts of fractionated Type 2 melt, and quench crystallization of groundmass minerals would account for the compositions of the Type 1 glass present, as illustrated in Figures 14 and S13–S18. We prefer open-system hybridization models over closed-system models because they better account for the chemical features of the glasses, such as the problems with K_2O concentrations, as discussed above. In either model, the observed negative correlation of H_2O and SiO_2

Table 3
Calculated Parental Liquids for Karoo Picrites

	Closed-system petrogenesis										
							Average calculated parental liquid			Average Lesotho tholeiite	
							$n = 6$			$n = 579$	
	KS-35A	KP-97[a]	KP-108[a]	KP-111	KP-142	KP-144[a]	Avg	Std dev	Range	Avg	Std dev
SiO_2	50.51	50.86	50.22	50.76	50.84	51.56	50.79	0.45	50–51	50.19	0.91
TiO_2	2.83	3.95	3.59	3.58	4.24	3.86	3.67	0.48	2.8–4.2	1.00	0.13
Al_2O_3	10.50	8.68	9.35	9.03	9.38	9.84	9.46	0.64	9–10.5	14.95	0.77
Cr_2O_3	0.09	0.11	0.00	0.06	0.04	0.12	0.07	0.05	0–0.1		
FeO	9.89	8.49	7.85	8.16	8.17	7.55	8.35	0.82	7.5–9.9	8.63	0.81
Fe_2O_3	1.32	1.43	1.64	1.19	1.22	1.29	1.35	0.17	1.2–1.6	1.69	0.16
MnO	0.17	0.14	0.14	0.14	0.13	0.13	0.14	0.01	0.1–0.2	0.18	0.02
MgO	9.52	9.77	9.14	9.94	9.13	8.52	9.34	0.52	9.1–9.9	6.86	1.24
CaO	9.09	7.67	8.00	7.56	7.33	7.78	7.91	0.62	7–9	10.33	0.70
Na_2O	2.02	0.33	2.82	1.70	1.29	1.60	1.63	0.82	0.3–2	2.13	0.36
K_2O	1.76	4.98	1.39	2.79	3.39	3.28	2.93	1.29	1.4–5	0.67	0.35
P_2O_5	0.42	0.66	0.65	0.62	0.63	0.59	0.60	0.09	0.4–0.7	0.17	0.03
H_2O^+	1.86	2.93	5.21	4.47	4.20	3.88	3.76	1.19	1.9–5.2	3.19	1.41
Total	100.00	100.00	100.00	100.00	100.00	100.00	100.00			100.00	
Mg#	63.19	67.22	67.46	68.46	64.82	66.80	66.33	1.95	63–75	58.37	4.49
$Na_2O + K_2O$	3.79	5.31	4.21	4.50	4.68	4.88	4.56	0.53	3.8–5	2.88	0.64
ppm											
Nb		36.27	28.33	30.49	31.39	38.25	32.95	4.15	28–30	7.19	2.89
Zr	318.78	476.98	504.52	507.38	615.38	533.25	492.71	97.51	320–615	96.85	17.78
Y	31.03	30.46	29.24	30.38	35.55	30.94	31.27	2.19	29–35	26.70	3.85
Sr	871.89	999.94	1236.73	1314.00	1720.88	1594.13	1289.59	328.79	870–1,720	191.25	42.21
Rb	38.00	94.25	86.67	113.63	63.00	59.63	75.86	27.36	60–114	14.51	17.22
Zn	116.11	93.32	56.70	84.53	98.18	111.36	93.37	21.38	56–116		
Cu	92.89	96.55	95.73	102.38	104.63	94.50	97.78	4.66	93–105	98.82	23.92
Ni	522.50	573.79	784.78	358.63	398.69	479.63	519.67	151.92	360–785	84.50	43.76
Co	72.83	88.50	135.83	74.25	72.00	78.75	87.03	24.67	72–135	44.73	5.77
Cr	671.33	683.27		340.15	299.79	759.25	550.76	213.84	300–760	254.26	104.53
V	259.67	229.87	200.52	226.13	241.88	202.50	226.76	22.80	200–260	252.84	31.04
Ba	704.06	965.45	1391.97	1298.25	1456.88	1485.00	1216.93	314.00	700–1,485	206.72	53.23
Sc	27.02	24.14	21.09	22.61	25.31	21.26	23.57	2.35	21–27	33.72	3.74
La		44.14	62.22	80.33	101.48	77.96	73.22	21.44	44–101	11.68	3.06
Ce		109.99	142.17	166.61	199.69	173.70	158.43	33.96	142–200	26.89	4.80
Pr		14.08	17.01	21.98	26.01	21.13	20.04	4.62	14–26		
Nd		64.82	70.89	89.44	103.28	84.49	82.58	15.25	65–103	14.62	8.04
Sm		11.241	12.406	15.975	18.259	14.063	14.39	2.80	11–18	3.86	0.77
Eu		3.138	3.144	4.320	4.973	3.679	3.85	0.79	3–5		
Gd		8.459	8.655	10.924	12.859	9.889	10.16	1.81	8–13	23.33	7.09
Tb		1.069	1.009	1.215	1.305	1.148	1.15	0.12	1.1–1.3	3.77	1.58
Dy		5.276	5.136	6.570	7.380	5.704	6.01	0.95	5–7	18.10	11.76

Table 3
Continued

	Closed-system petrogenesis										
							Average calculated parental liquid			Average Lesotho tholeiite	
							$n = 6$			$n = 579$	
	KS-35A	KP-97[a]	KP-108[a]	KP-111	KP-142	KP-144[a]	Avg	Std dev	Range	Avg	Std dev
Ho		0.908	0.970	1.125	1.238	0.934	1.03	0.14	0.9–1.2	3.36	2.36
Er		2.149	2.122	2.520	2.723	2.250	2.35	0.26	2.1–2.7	6.29	2.81
Tm		0.287	0.336		0.394	0.326	0.34	0.04	0.28–0.40	0.81	0.34
Yb		1.517	1.604	1.823	1.800	1.654	1.68	0.13	1.5–1.8	5.45	3.39
Lu		0.253		0.315	0.270	0.248	0.27	0.03	0.25–0.32	0.52	0.10
CIPW weight norm											
Quartz		2.76	1.99	2.50	4.47	4.46	0.09			**2.55**	
Plagioclase	32.09	10.59	34.36	24.23	21.59	24.44	22.91			48.47	
Orthoclase	10.58	30.32	8.69	17.26	20.92	20.15	18.21			4.22	
Diopside	23.09	21.66	22.49	20.70	18.79	20.61	20.96			14.96	
Hypersthene	25.02	22.97	21.06	24.69	22.24	19.06	27.32			23.65	
Olivine	0.58										
Ilmenite	5.47	7.73	7.18	7.12	8.39	7.62	6.89			1.96	
Magnetite	1.94	2.13	2.51	1.80	1.84	1.94	1.93			2.51	
Apatite	1.00	1.58	1.60	1.51	1.53	1.41	1.37			1.6	
Zircon	0.06	0.10	0.10	0.10	0.13	0.10	0.10			0.01	
Chromite	0.15	0.15	0.00	0.07	0.07	0.18	0.12			0.06	
	99.98	99.99	99.98	99.98	99.97	99.97	99.90			99.99	

	Open-system petrogenesis										
							Average calculated parental liquid			Average Lesotho tholeiite	
							$n = 6$			$n = 579$	
	Bulk g/m KS-35A	Bulk g/m- Type 2 glass KP-97	Bulk g/m KP-108	Bulk g/m- Type 2 glass KP-111	Bulk g/m KP-142	Bulk g/m KP-144	Avg	Std dev	Range	Avg	Std dev
SiO_2	51.04	51.97	51.48	48.71	51.85	51.96	51.17	1.25	49–52	50.19	0.91
TiO_2	2.97	4.33	3.92	5.30	4.66	4.00	4.20	0.78	3–5.3	**1.00**	0.13
Al_2O_3	11.04	9.44	10.21	9.38	10.37	10.15	10.10	0.62	9.4–11	14.95	0.77
Cr_2O_3	0.09	0.00	−0.13	0.00	−0.03	0.12	0.01	0.09			
FeO	9.62	8.26	6.28	11.20	7.54	6.75	8.27	1.86	6.3–11.2	8.63	0.81
Fe_2O_3	1.39	1.02	1.80	1.38	1.34	1.34	1.38	0.25	1–1.8	1.69	0.16
MnO	0.17	0.14	0.09	0.19	0.12	0.11	0.14	0.04	0.11–0.19	0.18	0.02
MgO	7.75	8.61	6.62	7.52	5.87	7.88	7.38	0.97	5.9–8.6	6.86	1.24
CaO	9.55	8.86	8.71	9.96	7.72	8.02	8.80	0.86	7.7–10	10.33	0.70
Na_2O	2.13	0.24	3.07	0.50	1.42	1.65	1.50	1.05	0.24–3.1	2.13	0.36
K_2O	1.85	5.40	1.52	3.90	3.77	3.40	3.31	1.43	1.9–5.4	0.67	0.35
P_2O_5	0.44	0.84	0.71	0.70	0.70	0.61	0.67	0.13	0.44–0.84	0.17	0.03
H_2O^+	1.96	0.90	5.71	1.25	4.66	4.02	3.08	1.98	0.9–5.7	3.19	1.41
Total	100.00	100.00	100.00	100.00	100.00	100.00	100.00			100.00	

Table 3
Continued

	Open-system petrogenesis										
							Average calculated parental liquid			Average Lesotho tholeiite	
							$n = 6$			$n = 579$	
	Bulk g/m KS-35A	Bulk g/m- Type 2 glass KP-97	Bulk g/m KP-108	Bulk g/m- Type 2 glass KP-111	Bulk g/m KP-142	Bulk g/m KP-144	Avg	Std dev	Range	Avg	Std dev
Mg#	58.93	65.01	65.26	54.46	58.13	67.55	61.56	5.11	54–68	58.37	4.49
$Na_2O + K_2O$	3.99	5.64	4.62	4.40	5.25	5.05	4.83	0.60	4.0–5.6	2.88	0.64
ppm											
Nb		10.05	34.76	20.85	34.88	42.50	28.61	12.99	10–43	7.19	2.89
Zr	335.56	328.35	619.05	438.58	683.75	592.50	499.63	152.82	336–684	96.85	17.78
Y	32.67	15.33	35.87	30.46	39.50	34.38	31.37	8.43	15–40	26.70	3.85
Sr	917.78	843.68	1517.46	381.26	1905.75	1771.25	1222.86	599.83	381–1906	191.25	42.21
Rb	40.00	73.75	106.35	87.16	70.00	66.25	73.92	22.14	40–106	14.51	17.22
Zn	122.22		7.41		87.35	123.73	85.18	54.50	7–123		
Cu	97.78		117.46		116.25	105.00	109.12	9.42	98–117	98.82	23.92
Ni	550.00		263.56		179.38	180.25	293.30	175.63	180–550	84.50	43.76
Co	76.67		166.67		80.00	87.5	102.71	42.88	77–167	44.73	5.77
Cr	706.67		−862.19		−99.43	818.5	140.89	783.83		254.26	104.53
V	273.33		246.03		268.75	225	253.28	22.31	225–273	252.84	31.04
Ba	741.11	931.98	1707.94	952.40	1618.75	1650	1267.03	436.49	741–1708	206.72	53.23
Sc	28.44	20.41	25.87	25.45	28.13	23.63	25.32	3.00	20–28	33.72	3.74
La		30.77	76.35	65.97	112.75	86.63	74.49	29.99	30–113	11.68	3.06
Ce		66.05	174.44	158.03	221.88	193.00	162.68	58.99	66–222	26.89	4.80
Pr		6.37	20.87	20.43	28.90	23.48	20.01	8.34	6–29		
Nd		37.53	86.98	91.05	114.75	93.88	84.84	28.54	38–115	14.62	8.04
Sm		4.72	15.22	16.81	20.29	15.63	14.53	5.84	5–20	3.86	0.77
Eu		1.18	3.86	4.23	5.53	4.09	3.78	1.59	1–5		
Gd		2.86	10.62	11.08	14.29	10.99	9.97	4.24	3–14	23.33	7.09
Tb		0.35	1.24	1.49	1.45	1.28	1.16	0.46	0.4–1.5	3.77	1.58
Dy		1.83	6.30	7.73	8.20	6.34	6.08	2.52	2–8	18.10	11.76
Ho		0.35	1.19	1.29	1.38	1.04	1.05	0.41	0.4–1.4	3.36	2.36
Er		0.95	2.60	3.45	3.03	2.50	2.51	0.95	1–3	6.29	2.81
Tm		0.08	0.41	0.42	0.44	0.36	0.34	0.15	0.1–0.4	0.81	0.34
Yb		0.66	1.97	2.65	2.00	1.84	1.82	0.73	0.7–2.7	5.45	3.39
Lu		0.10		0.35	0.30	0.28	0.26	0.11	0.1–0.4	0.52	0.10
CIPW weight norm											
Quartz	1.70	3.45	6.06	2.35	8.68	5.60	4.62			2.55	
Plagioclase	33.12	10.76	37.63	16.06	23.89	25.22	24.49			48.47	
Orthoclase	10.93	31.91	9.51	23.05	23.34	20.92	20.15			4.22	
Diopside	23.95	23.85	24.42	26.85	19.34	21.21	23.43			14.96	
Hypersthene olivine	19.47	17.45	9.84	16.69	11.57	15.33	15.28			23.65	
Ilmenite	5.64	8.22	7.88	10.07	9.27	7.90	8.22			1.96	
Magnetite	2.02	1.48	2.75	2.00	2.03	2.02	2.06			2.51	

Table 3
Continued

	Open-system petrogenesis										
							Average calculated parental liquid			Average Lesotho tholeiite	
							$n = 6$			$n = 579$	
	Bulk g/m KS-35A	Bulk g/m- Type 2 glass KP-97	Bulk g/m KP-108	Bulk g/m- Type 2 glass KP-111	Bulk g/m KP-142	Bulk g/m KP-144	Avg	Std dev	Range	Avg	Std dev
Apatite	1.02	1.95	1.74	1.62	1.69	1.46	1.60			1.6	
Zircon	0.07	0.06	0.13	0.09	0.15	0.12	0.10			0.01	
Chromite	0.15					0.18				0.06	
	98.07	99.13	99.96	98.78	99.96	99.96	99.95			99.99	

[a]Parental liquid compositions adjusted by subtracting 1% increments of equilibrium olivine until liquid reaches Fe-Mg equilibrium.

(Figure 6b) may be indicative of progressive degassing of the residual melts during crystallization, with the released fluid having caused variable serpentinization of olivine phenocrysts.

5.4. Mantle Sources, Origin of Parental Liquids, and Crustal Contamination

A variety of mantle and crustal sources have been proposed to account for the compositional and isotopic ranges displayed by the multiplicity of magmatic rocks in the Karoo LIP (e.g., Hawkesworth et al., 1984; Heinonen et al., 2016; Kamenetsky et al., 2017; Turunen et al., 2019). Evaluating the role of crustal contamination for incompatible element enrichment of mantle-derived rocks typically relies on radiogenic and stable isotope measurements, which are regrettably lacking for the picritic rocks we studied. However, on the basis of combined geochemical and isotopic data, several studies have concluded that similar enriched Karoo picrites as well as other high-Ti magmatic rocks were sourced mainly or entirely from the subcontinental lithospheric mantle (SCLM), with minimal effects of crustal contamination (e.g., Bristow et al., 1984; Ellam & Cox, 1989; Jourdan et al., 2007; Luttinen, 2018; Riley et al., 2005; Sweeney et al., 1994). In any case, our calculated parental liquids for both closed-system and open-system petrogenesis are extraordinarily enriched in incompatible trace elements (e.g., average Sr = 1,222–1,290 ppm, Ba = 1,216–1,267 ppm, Zr = 493–500 ppm, Table 3), with values far higher than almost all typical continental crustal rock types (upper continental crust, Sr = 320 ppm, Ba = 624 ppm, Zr = 193 ppm, Rudnick & Gao, 2003). This enrichment, therefore, must be an inherent property of these melts, with or without crustal contamination. Harris et al. (2015) concluded that the high $\delta^{18}O$ values of Karoo enriched high-Ti picrites, similar to those studied here, could not be explained by crustal contamination, but instead requires a high $\delta^{18}O$ mantle source. Finally, Ellam et al. (1992) argued on the basis of Os isotopes that both the low $^{187}Os/^{188}Os$ values and the enrichments in incompatible elements for Karoo picrites are strong indicators of SCLM sources, and that crustal contamination effects were unlikely. We concur with those authors who conclude that the low-volume, high-Ti Karoo magmatic rocks, including the alkali picrites in this study, were sourced mainly or entirely from the SCLM. Ashwal (2017) argued on the basis of volume constraints that the enormous quantity of low-Ti Karoo tholeiites cannot have been sourced from the SCLM, but instead were generated from sublithospheric (i.e., plume) sources (see also Luttinen, 2018). Credible arguments have been put forward, however, that both the low-Ti and high-Ti magmatic suites in continental LIPs were derived from sublithospheric (i.e., deep mantle plume) sources (e.g., Campbell, 2007; Zhou et al., 2008), but it is not clear if such models can account for the extreme incompatible element enrichments in high-Ti picrites and related rocks or the relative volumes of the two suites. The high-Ti picrites also have distinctly lower Nb concentrations and Nb/La and Nb/Zr ratios compared to plume-derived ocean-island alkali basalts (White, 2010, 2020), which argues against a sublithospheric source.

Several studies have concluded that the enriched picritic rocks of the Karoo LIP owe their origin to hybridization and blending of two distinct components (Ellam & Cox, 1991; Ellam et al., 1992; Heinonen

et al., 2016; Luttinen, 2018; Neumann et al., 2011). Most models involve mixing of low-Ti tholeiitic magmas derived from sublithospheric sources with highly enriched melts sourced from the SCLM. The model of open-system petrogenesis that we described above for the studied picrites represents an example of such hybridization, and the petrographic and geochemical properties of our samples may have preserved unique evidence for this. However, our calculations of parent melts show that the compositions of both the earlier melt surrounding olivine phenocrysts and the later infiltrating melt are similar, with both exhibiting incompatible element enrichment levels much higher than average low-Ti tholeiitic basalts (Table 3 and Figure 11b). The most significant elemental variability between the two melts (and which is inherited by Type 1 vs. Type 2 glasses) is for Rb, Ba, K, and Sr (Figure 10), which may be attributable to differences in restite mineralogy (discussed below) of an otherwise similar mantle source. This implies that the Karoo alkali picrites are hybrid rocks representing mixtures of crystals and melts from different magmas, both of which were derived from the SCLM.

The bulk of the SCLM below the Kaapvaal Craton must be depleted, cold, buoyant, stable, and infertile, having been formed by massive extraction of basaltic and komatiitic magmas during the early-Archean to mid-Archean (e.g., de Wit et al., 1992; Kamber & Tomlinson, 2019). This is supported by studies involving seismic imaging (e.g., Fouch et al., 2004) and petrology of kimberlite xenolith suites (e.g., Carlson et al., 2000; Pearson et al., 1995). If the incompatible-rich, high-Ti Karoo magmas were derived from SCLM, their sources, therefore, must be relatively small-volume enriched domains, representing either ancient subducted crustal materials (e.g., oceanic crust) or local regions metasomatized by fluids or melts. The properties of our calculated parental liquids to the picritic rocks we studied that are relevant to characterizing their mantle sources include: high MgO, TiO_2, K_2O, P_2O_5, and H_2O, low Al_2O_3, CaO, and Na_2O, and very high Sr, Rb, Ba, Zr, LREE, and La/Yb, relative to the average low-Ti tholeiitic basalt (Table 3). Several studies have concluded that picritic rocks similar to those studied here were derived from pyroxene-rich (pyroxenite or eclogite) rather than peridotitic sources (e.g., Harris et al., 2015; Heinonen & Luttinen. 2008; Howarth & Harris, 2017; Kamenetsky et al., 2017). The high NiO (average = 0.36–0.48 wt. %), low CaO (average = 0.23–0.27 wt. %) and low MnO (average = 0.16–0.23 wt. %) of olivine phenocrysts in our samples (Table S1) also support a nonperidotitic source (Howarth & Harris, 2017; Kamenetsky et al., 2017; Sobolev et al., 2007). A garnet-bearing source, with garnet having been retained after partial melting, is supported by a variety of major and trace element ratios (Jourdan et al., 2007; Kamenetsky et al., 2017). Melting of clinopyroxene-rich sources was invoked to account for the Sr-rich alkali picrites of West Greenland by Larsen et al. (2003), citing evidence that clinopyroxenes in metasomatized mantle xenoliths may contain up to 600 ppm Sr and 200 ppm Ce. The high K_2O, H_2O, Rb, and Ba in our calculated parental melts may be an indicator of pargasitic amphibole and/or phlogopite in their mantle sources, and possibly the presence of metasomatic Ba-Ti titanites like lindsleyite ($Ba[Ti, Cr, Fe, Zr, Mg]_{21}O_{38}$) and hawthornite ($Ba[Ti, Cr, Fe, Mg]_{12}O_{19}$) (Haggerty et al., 1983) may also have played a role. In any case, the nature of the alkali picrites we studied as mixtures of accumulated olivine phenocrysts and variably evolved residual melts produced by extensive fractional crystallization, with or without infiltration of genetically unrelated melts, argues against the commonly held perception that these picrites represent some of the most primitive of melts in the Karoo LIP (e.g., Bristow et al., 1984; Cox & Jamieson, 1974; Harris et al., 2015).

Alternatively, our calculated parental liquids may themselves represent derivatives of more primitive, more mafic melts, resulting from an unquantifiable extent of olivine fractionation. Experimental work shows that olivine fractionation from deep, near-solidus komatiitic melts, derived from a garnet lherzolite source, may produce enriched alkali picrite liquids (Milholland & Presnall, 1998). In such a scenario, the garnet lherzolite source, situated in the lower SCLM, must also be enriched in incompatible trace elements. In either case, we envisage the primitive or parental liquids that gave rise to the alkali picritic rocks we studied to have been formed by low degrees of partial melting of enriched domains in the sub-Kaapvaal SCLM.

The enrichments in MgO, incompatible elements and volatile components in these rocks, their parental melts and mantle sources are suggestive of a possible link with other small-volume magmatic rocks, such as kimberlites, lamproites, and carbonatites. Like our alkali picrites, both Group I ("basaltic") and Group II ("micaceous") kimberlites are markedly enriched in volatiles and incompatible elements (e.g., average Sr = 1,295–1,869 ppm, Ba = 1,380–3,799 ppm, Zr = 371–399 ppm, Becker & le Roex, 2006). In the kimberlite database of Tappe et al. (2018) there are about a dozen kimberlite occurrences with ages of ~180 Ma scat-

tered throughout southern Africa, which could be products of the Karoo LIP. As with LIP magmatism, there is considerable disagreement as to the nature of kimberlite mantle sources, with some favoring derivation from sublithospheric sources (e.g., Arndt, 2003; Ringwood et al., 1992) and others favoring SCLM derivation (e.g., Becker & le Roex, 2006; Tainton & McKenzie, 1994). A link between LIPs and carbonatites was discussed in general terms by Ernst and Bell (2010), and by Natali et al. (2018) for the Paraná-Etendeka LIP. There are small occurrences of Karoo-age carbonatite, with associated ijolite and nephelinite in the Buhera district, SE Zimbabwe (Harmer et al., 1998). Lamproites that slightly post-date Karoo basalts in Dronning Maud Land, Antarctica were described by Luttinen et al. (2002). A direct petrogenetic relationship between these magmatic rocks and the alkali picrites studied here is uncertain, although their mantle sources may share some properties such as enrichment in alkalies, incompatible elements, MgO, TiO_2, and volatiles. An important difference is that CO_2 is an important component in kimberlites, lamproites and carbonatites, whereas our results show that it is nearly absent in the picrites we studied.

6. Conclusions

High-Ti Karoo picrites from the Letaba Formation are unusually enriched in incompatible major and trace elements, considering their high modal olivine content. The incompatible elements reside in evolved trachytic to dacitic glasses and/or feldspars, where present; glasses contain up to 3.9 wt. % H_2O, but little to no CO_2.

Some samples contain two coexisting, compositionally distinct glasses, whose compositions correlate with textural associations: minor volumes of Type 2 glass adjacent to olivine phenocrysts have distinctly lower K_2O, MgO and FeO, higher H_2O, and much higher Na_2O and Sr, relative to the dominant Type 1 glass phases in the groundmasses. Type 2 glasses can be attributed to removal of olivine components from resident residual melts, and the larger volumes of Type 1 glasses in the groundmasses represent residual melts after quench crystallization of clinopyroxene, ilmenite, and apatite. The compositional data and textural observations are best interpreted in terms of an open-system petrogenetic model in which olivine phenocrysts accumulated in an evolved, Sr-rich melt, now represented by Type 2 glasses. This crystal-rich slurry was infiltrated by compositionally distinct melts, represented by bulk groundmass compositions. Our glassy picrite samples thus represent unique examples of the magmatic hybridization processes that have often been proposed based on isotopic relationships. They should not be considered as inherently primitive magmatic rocks.

Fractional crystallization modeling yields evolved residual liquids that match both glass compositions, as well as liquid evolution trajectories based on mass-balance calculations involving mineral and bulk groundmass compositions. This allows estimation of liquid lines of descent and parental melt compositions by mass balance. Calculated parental melts are enriched in MgO and K_2O, as well as almost all incompatible trace elements, relative to average low-Ti tholeiites that represent the vastly dominant volumes of magmas in the Karoo LIP.

We interpret the high-Ti, incompatible-rich Karoo picrites as having formed by small degrees of partial melting of pyroxene and garnet-bearing domains within the SCLM underlying the Kaapvaal Craton that are enriched in Sr and other large-ion lithophile elements. Compositions of the parental magmas and putative mantle source regions are suggestive of a possible link with other small-volume, incompatible-rich magmatic rocks such as kimberlites, lamproites, and carbonatites.

Data Availability Statement

Frédéric Couffignal is thanked for his skillful operation of the Cameca 1280 SIMS instrument at GFZ Potsdam along with its virtual link to Johannesburg. Uwe Dittmann in Potsdam provided the high-quality SIMS mounts needed for our H and C determinations and Michael Wiedenbeck provided useful input on the data evaluation. Critical comments by Ben Hayes on an earlier version of the manuscript were extremely helpful, as were the reviews by Nick Arndt, Chris Hawkesworth, Vadim Kamenetsky, and Arto Luttinen. Data sets for this research have been archived in the EarthChem Library data repository and can be accessed at: https://doi.org/10.26022/IEDA/111904.

Acknowledgments
We thank Chris Harris for providing samples and Niyko Shingange, who completed his B.Sc. Honors project relating to this subject of this paper at the University of the Witwatersrand. RB acknowledges funding through a National Research Foundation (NRF) National Equipment Project (NEP) grant (UID-105674) to establish the LA-ICPMS facility at the University of the Witwatersrand. This work was supported by a generous grant from the Oppenheimer Memorial Trust and by research funds from the South African NRF.

References

Anders, E., & Grevesse, N. (1989). Abundances of the elements: Meteoritic and solar. *Geochimica et Cosmochimica Acta*, *53*, 197–214. https://doi.org/10.1016/0016-7037(89)90286-x

Arndt, N. (2003). Komatiites, kimberlites, and boninites. *Journal of Geophysical Research*, *108*(B6), 2293. https://doi.org/10.1029/2002JB002157

Ashwal, L. D. (2017). *Mantle sources and origin of the four overlapping continental LIPs generated throughout 2500 m.y. of Kaapvaal Craton history in southern Africa*. Abstract V34B-01, Paper presented at 2017 Fall Meeting, American Geophysical Union, New Orleans, Louisiana, 11-15 December, 2017.

Barnes, S. J., & Kunilov, V. Y. (2000). Spinels and Mg ilmenites from the Noril'sk 1 and Talnakh intrusions and other mafic rocks of the Siberian Flood Basalt Province. *Economic Geology*, *95*, 1701–1717. https://doi.org/10.2113/gsecongeo.95.8.1701

Barnes, S. J., & Roeder, P. L. (2001). The range of spinel compositions in terrestrial mafic and ultramafic rocks. *Journal of Petrology*, *42*, 2279–2302. https://doi.org/10.1093/petrology/42.12.2279

Becker, M., & le Roex, A. P. (2006). Geochemistry of South African on- and off-craton, Group I and Group II kimberlites: Petrogenesis and source region evolution. *Journal of Petrology*, *47*, 673–703. https://doi.org/10.1093/petrology/egi089

Boudreau, A. E. (1999). PELE-a version of the MELTS software program for the PC platform. *Computers and Geosciences*, *25*, 201–203. https://doi.org/10.1016/s0098-3004(98)00117-4

Bristow, J. W. (1980). *The geochronology and geochemistry of Karoo volcanics in the Lebombo and adjacent areas* (PhD thesis, 74 pp.). Town, South Africa: University of Cape.

Bristow, J. W. (1984). Picritic rocks of the north Lebombo and south-east Zimbabwe. In A. J. Erlank (Ed.), Petrogenesis of the volcanic rocks of the Karoo province (Vol. 13, pp. 105–123). Geological Society of South Africa Special Publication.

Bristow, J. W., Allsopp, H. L., Erlank, A. J., Marsh, J. S., & Armstrong, R. A. (1984). Strontium isotope characterization of Karoo volcanic rocks. In A. J. Erlank (Ed.), Petrogenesis of the volcanic rocks of the Karoo province (Vol. 13, pp. 295–329). Geological Society of South Africa Special Publication.

Buiter, S. J. H., & Torsvik, T. H. (2014). A review of Wilson cycle plate margins: A role for mantle plumes in continental break-up along sutures? *Gondwana Research*, *26*, 627–653. https://doi.org/10.1016/j.gr.2014.02.007

Campbell, I. H. (2007). Testing the plume theory. *Chemical Geology*, *241*, 153–176. https://doi.org/10.1016/j.chemgeo.2007.01.024

Carlson, R. W., Boyd, F. R., Shirey, S. B., Janney, P. E., Grove, T. L., Bowring, S. A., et al. (2000). Continental growth, preservation and modification in southern Africa. *Geological Society of America Today*, *20*, 1–7.

Cawthorn, R. G., Bristow, J. W., & Groves, D. I. (1989). Magnesian ilmenite in picritic basalts from the Karoo Province, South Africa. *Mineralogical Magazine*, *53*, 245–252. https://doi.org/10.1180/minmag.1989.053.370.12

Cleverly, R. W., & Bristow, J. W. (1979). Revised volcanic stratigraphy of the Lebombo monocline. *South African Journal of Geology*, *82*, 227–230.

Cox, K. G. (1988). The Karoo Province. In J. D. Macdougall (Ed.), *Continental flood basalts* (pp. 239–271). Dordrecht: Kluwer.

Cox, K. G., & Hawkesworth, C. J. (1985). Geochemical stratigraphy of the Deccan Traps at Mahabaleshwar, Western Ghats, India, with implications for open system magmatic processes. *Journal of Petrology*, *26*, 355–377. https://doi.org/10.1093/petrology/26.2.355

Cox, K. G., & Jamieson, B. G. (1974). The olivine-rich lavas of Nuanetsi: A study of polybaric magmatic evolution. *Journal of Petrology*, *15*, 269–301. https://doi.org/10.1093/petrology/15.2.269

Cox, K. G., Johnson, R. L., Monkman, L. J., Stillman, C. J., Vail, J. R., & Wood, D. N. (1965). The geology of the Nuanetsi Igneous Province. *Philosophical Transactions of the Royal Society of London-Series A: Mathematical and Physical Sciences*, *257*, 71–218.

Cox, K. G., Macdonald, R., & Horning, G. (1967). Geochemical and petrographic provinces in the Karroo basalts of southern Africa. *American Mineralogist*, *52*, 1451–1474.

de Wit, M. J., de Ronde, C. E. J., Tredoux, M., Roering, C., Hart, R. J., Armstrong, R. A., et al. (1992). Formation of an Archaean continent. *Nature*, *357*, 553–562. https://doi.org/10.1038/357553a0

Duncan, A. R., Erlank, A. J., & Marsh, J. S. (1984). Regional geochemistry of the Karoo igneous province. In A. J. Erlank (Ed.), Petrogenesis of the volcanic rocks of the Karoo province (Vol. 13, pp. 355–388). Geological Society of South Africa Special Publication.

Elkins, L. T., & Grove, T. L. (1990). Ternary feldspar experiments and thermodynamic models. *American Mineralogist*, *75*, 544–559.

Ellam, R. M., Carlson, R. W., & Shirey, S. B. (1992). Evidence from Re-Os isotopes for plume-lithosphere mixing in Karoo flood basalt genesis. *Nature*, *359*, 718–721. https://doi.org/10.1038/359718a0

Ellam, R.M., & Cox, K. G. (1989). A Proterozoic lithospheric source for Karoo magmatism: evidence from Nuanetsi picrites. *Earth and Planetary Science Letters*, *92*, 207–218.

Ellam, R. M., & Cox, K. G. (1991). An interpretation of Karoo picrite basalts in terms of interaction between asthenospheric magmas and the mantle lithosphere. *Earth and Planetary Science Letters*, *105*, 330–342. https://doi.org/10.1016/0012-821x(91)90141-4

Erlank, A. J. (Ed.) (1984). Petrogenesis of the volcanic rocks of the Karoo province (Vol. *13*, 388 pp.). Geological Society of South Africa Special Publication.

Ernst, R. E. (2014). *Large Igneous Provinces* (653 pp.). Cambridge, UK: Cambridge University Press.

Ernst, R. E., & Bell, K. (2010). Large igneous provinces (LIPs) and carbonatites. *Mineralogy and Petrology*, *98*, 55–76. https://doi.org/10.1007/s00710-009-0074-1

Ernst, R. E., & Buchan, K. L. (1997). Giant radiating dyke swarms: Their use in identifying Pre-Mesozoic Large Igneous Provinces and mantle plumes. In J. J. Mahoney, & M. F. Coffin (Eds.), *Large Igneous provinces: Continental, oceanic and planetary flood volcanism. Geophysical Monograph 100* (pp. 297–333). Washington, DC: American Geophysical Union.

Fedorenko, V. A., Lightfoot, P. C., Naldrett, A. J., Czamanske, G. K., Hawkesworth, C. J., Wooden, J. L., & Ebel, D. S. (1996). Petrogenesis of the flood-basalt sequence at Noril'sk, North Central Siberia. *International Geology Review*, *38*, 99–135. https://doi.org/10.1080/00206819709465327

Fouch, M. J., James, D. E., VanDecar, J. C., van der Lee, S., & the Kaapvaal Seismic Group. (2004). Mantle seismic structure beneath the Kaapvaal and Zimbabwe Cratons. *South African Journal of Geology*, *107*, 33–44. https://doi.org/10.2113/107.1-2.33

Gao, S., Liu, X., Yuasn, H., Hattendorf, B., Günther, D., Chen, L., & Hu, S. (2002). Determination of forty two major and trace elements in USGS and NIST SRM glasses by laser ablation-inductively coupled plasma-mass spectrometry. *Geostandards Newsletter*, *26*, 181–196.

Ghiorso, M. S., & Sack, R. O. (1995). Chemical mass transfer in magmatic processes IV. A revised and internally consistent thermodynamic model for the interpolation and extrapolation of liquid-solid equilibria in magmatic systems at elevated temperatures and pressures. *Contributions to Mineralogy and Petrology*, *119*, 197–212. https://doi.org/10.1007/bf00307281

Gibson, S. A., Thompson, R. N., Dickin, A. P., & Leonardos, O. H. (1995). High-Ti and low-Ti mafic potassic magmas: Key to plume-lithosphere interactions and continental flood-basalt genesis. *Earth and Planetary Science Letters*, *136*, 149–165. https://doi.org/10.1016/0012-821x(95)00179-g

Haggerty, S. E., Smyth, J. R., Erlank, A. J., Rickard, R. S., & Danchin, R. V. (1983). Lindsleyite (Ba) and mathiasite (K): Two new chromium-titanates in the crichtonite series from the upper mantle. *American Mineralogist*, *68*, 494–505.

Harmer, R. E., Lee, C. A., & Eglington, B. M. (1998). A deep mantle source for carbonatite magmatism: Evidence from the nephelinites and carbonatites of the Buhera district, SE Zimbabwe. *Earth and Planetary Science Letters*, *158*, 131–142. https://doi.org/10.1016/s0012-821x(98)00053-3

Harris, C., le Roux, P., Cochrane, R., Martin, L., Duncan, A. R., Marsh, J. S., et al. (2015). The oxygen isotope composition of Karoo and Etendeka picrites: High $\delta^{18}O$ mantle or crustal contamination? *Contributions to Mineralogy and Petrology*, *170*, 8. https://doi.org/10.1007/s00410-015-1164-1

Harris, C., Marsh, J. S., Duncan, A. R., & Erlank, A. J. (1990). The petrogenesis of the Kirwan basalts of Dronning Maud Land, Antarctica. *Journal of Petrology*, *31*, 341–369. https://doi.org/10.1093/petrology/31.2.341

Hawkesworth, C. J., Lightfoot, P. C., Fedorenko, V. A., Blake, S., Naldrett, A. J., Doherty, W., & Gorbachev, N. S. (1995). Magma differentiation and mineralisation in the Siberian continental flood basalts. *Lithos*, *34*, 61–88. https://doi.org/10.1016/0024-4937(95)90011-x

Hawkesworth, C. J., Marsh, J. S., Duncan, A. R., Erlank, A. J., & Norry, M. J. (1984). The role of continental lithosphere in the generation of the Karoo volcanic rocks: Evidence from combined Nd- and Sr-isotope studies. In A. J. Erlank (Ed.), Petrogenesis of the volcanic rocks of the Karoo province (Vol. 13, pp. 341–354). Geological Society of South Africa Special Publication.

Heinonen, J. S., & Luttinen, A. V. (2008). Jurassic dikes of Vestfjella, western Dronning MAUD Land, Antarctica: Geochemical tracing of ferropicrite sources. *Lithos*, *105*, 347–364. https://doi.org/10.1016/j.lithos.2008.05.010

Heinonen, J. S., Luttinen, A. V., & Bohrson, W. A. (2016). Enriched continental flood basalts from depleted mantle melts: Modeling lithospheric contamination of Karoo lavas from Antarctica. *Contributions to Mineralogy and Petrology*, *171*. https://doi.org/10.1007/s00410-015-1214-8

Howarth, G. H., & Harris, C. (2017). Discriminating between pyroxenite and peridotite sources for continental flood basalts (CFB) in southern Africa using olivine chemistry. *Earth and Planetary Science Letters*, *475*, 143–151. https://doi.org/10.1016/j.epsl.2017.07.043

Jochum, K.P., Weis, U., Stall, B., Kuzmin, D., Yang, Q., Raczek, I., et al. (2011). Determination of reference values for NIST SRM 610-617 glasses following ISO guidelines. *Geostandards and Geoanalytical Research*, *35*, 397–429.

Jourdan, F., Bertrand, H., Schärer, U., Blichert-Toft, J., Féraud, G., & Kampunzu, A. B. (2007). Major and trace element and Sr, Nd, Hf, and Pb isotope compositions of the Karoo Large Igneous Province, Botswana-Zimbabwe: Lithosphere vs mantle plume contribution. *Journal of Petrology*, *48*, 1043–1077. https://doi.org/10.1093/petrology/egm010

Jourdan, F., Féraud, G., Bertrand, H., Watkeys, M. K., & Renne, P. R. (2008). The $^{40}Ar/^{39}Ar$ ages of the sill complex of the Karoo Large Igneous Province: Implications for the Pliensbachian-Toarcian climate change. *Geochemistry, Geophysics, Geosystems*, *9*, Q06009. https://doi.org/10.1029/2008GC001994

Kamber, B. S., & Tomlinson, E. L. (2019). Petrological, mineralogical and geochemical peculiarities of Archaean cratons. *Chemical Geology*, *511*, 123–151. https://doi.org/10.1016/j.chemgeo.2019.02.011

Kamenetsky, V. S., Maas, R., Kamenetsky, M. B., Yaxley, G. M., Ehrig, K., Zellmer, G. F., et al. (2017). Multiple mantle sources of continental magmatism: Insights from "high-Ti" picrites of Karoo and other large igneous provinces. *Chemical Geology*, *455*, 22–31. https://doi.org/10.1016/j.chemgeo.2016.08.034

Larsen, L. M., Pedersen, A. K., Sundvoll, B., & Frei, R. (2003). Alkali picrites formed by melting of old metasomatized lithospheric mantle: Manitdlat member, Vaigat Formation, Palaeocene of West Greenland. *Journal of Petrology*, *44*, 3–38. https://doi.org/10.1093/petrology/44.1.3

Luttinen, A. V. (2018). Bilateral geochemical asymmetry in the Karoo Large Igneous Province. *Scientific Reports*, *8*, 5223. https://doi.org/10.1038/s41598-018-23661-3

Luttinen, A. V., & Furnes, H. (2000). Flood basalts of Vestfjella: Jurassic magmatism across an Archaean-Proterozoic lithospheric boundary in Dronning Maud Land, Antarctica. *Journal of Petrology*, *41*, 1271–1305. https://doi.org/10.1093/petrology/41.8.1271

Luttinen, A. V., Leat, P. T., & Furnes, H. (2010). Björnnutane and Sembberget basalt lavas and the geochemical provinciality of Karoo magmatism in western Dronning Maud Land, Antarctica. *Journal of Volcanology and Geothermal Research*, *198*, 1–18. https://doi.org/10.1016/j.jvolgeores.2010.07.011

Luttinen, A. V., Zhang, X., & Foland, K. A. (2002). 159 Ma Kjakebeinet lamproites (Dronning Maud Land, Antarctica) and their implications for Gondwana breakup processes. *Geological Magazine*, *139*, 525–539. https://doi.org/10.1017/s001675680200674x

Macdougall, J. D. (Ed.) (1988). *Continental flood basalts* (341 pp.). Dordrecht: Kluwer.

Mahoney, J. J., & Coffin, M. F. (Eds.) (1997). *Large Igneous provinces: Continental, oceanic and planetary flood volcanism. Geophysical Monograph 100* (438 pp.). Washington, DC: American Geophysical Union.

Marsh, J. S., Ewart, A., Milner, S. C., Duncan, A. R., & Miller, R. M. (2001). The Etendeka Igneous Province: Magma types and their stratigraphic distribution with implications for the evolution of the Paraná-Etendeka flood basalt province. *Bulletin of Volcanology*, *62*, 464–486. https://doi.org/10.1007/s004450000115

Marsh, J. S., Hooper, P. R., Rehacek, J., Duncan, A., & Duncan, A. R. (1997). Stratigraphy and age of Karoo basalts of Lesotho and implications for correlations within the Karoo Igneous Province. In J. J. Mahoney, & M. F. Coffin (Eds.), *Large Igneous provinces: Continental, oceanic and planetary flood volcanism. Geophysical Monograph 100* (pp. 247–272). Washington, DC: American Geophysical Union.

Melluso, L., Barbieri, M., & Beccaluva, L. (2004). Chemical evolution, petrogenesis, and regional chemical correlations of the flood basalt sequence in the central Deccan Traps, India. *Journal of Earth System Science*, *113*, 587–603. https://doi.org/10.1007/bf02704024

Milholland, C. S., & Presnall, D. C. (1998). Liquidus phase relations in the $CaO-MgO-Al_2O_3-SiO_2$ system at 3.0 GPa: The aluminous pyroxene thermal divide and high-pressure fractionation of picritic and komatiitic magmas. *Journal of Petrology*, *39*, 3–27. https://doi.org/10.1093/petroj/39.1.3

Morgan, G. B., & London, D. (1996). Optimizing the electron microprobe analysis of hydrous alkali aluminosilicate glasses. *American Mineralogist*, *81*, 1176–1185. https://doi.org/10.2138/am-1996-9-1016

Natali, C., Beccaluva, L., Bianchini, G., & Siena, F. (2017). Comparison among Ethiopia-Yemen, Deccan, and Karoo continental flood basalts of central Gondwana: Insights on lithosphere versus asthenosphere contributions in compositionally zoned magmatic provinces. In G. Bianchini, K.-L. Bodiner, R. Braga, & M. Wilson (Eds.), *The crust-mantle and lithosphere-asthenosphere boundaries: Insights from xenoliths, orogenic deep sections, and geophysical studies*. Geological Society of South Africa Special Publication Paper 526. https://doi.org/10.1130/2017.2526(10)

Natali, C., Beccaluva, L., Bianchini, G., & Siena, F. (2018). Coexistence of alkaline-carbonatite complexes and high-MgO CFB in the Paranà-Etendeka province: Insights on plume-lithosphere interactions in the Gondwana realm. *Lithos*, *296–299*, 54–66. https://doi.org/10.1016/j.lithos.2017.11.001

Neumann, E.-R., Svensen, H., Galerne, C. Y., & Planke, S. (2011). Multistage evolution of dolerites in the Karoo Large Igneous Province, central South Africa. *Journal of Petrology*, *52*, 959–984. https://doi.org/10.1093/petrology/egr011

Paton, C., Hellstrom, J., Paul, B., Woodhead, J., & Hergt, J. (2011). Iolite: Freeware for the visualisation and processing of mass spectrometric data. *Journal of Analytical Atomic Spectrometry*, *26*(12), 2508–2518. https://doi.org/10.1039/c1ja10172b

Paton, C., Woodhead, J. D., Hellstrom, J. C., Hergt, J. M., Greig, A., & Maas, R. (2010). Improved laser ablation U-Pb zircon geochronology through robust downhole fractionation correction. *Geochemistry, Geophysics, Geosystems*, *11*, Q0AA06. https://doi.org/10.1029/2009GC002618

Pearson, D. G., Carlson, R. W., Shirey, S. B., Boyd, F. R., & Nixon, P. H. (1995). Stabilisation of Archaean lithospheric mantle: A ReOs isotope study of peridotite xenoliths from the Kaapvaal craton. *Earth and Planetary Science Letters*, *134*, 341–357. https://doi.org/10.1016/0012-821x(95)00125-v

Peate, D. W., Hawkesworth, C. J., & Mantovani, M. S. M. (1992). Chemical stratigraphy of the Paraná lavas (South America): Classification of magma types and their spatial distribution. *Bulletin of Volcanology*, *55*, 119–139. https://doi.org/10.1007/bf00301125

Riley, T. R., Leat, P. T., Curtis, M. L., Millar, I. L., Duncan, R. A., & Fazel, A. (2005). Early-Middle Jurassic dolerite dykes from Western Dronning Maud Land (Antarctica): Identifying mantle sources in the Karoo Large Igneous Province. *Journal of Petrology*, *46*, 1489–1524. https://doi.org/10.1093/petrology/egi023

Ringwood, A. E., Kesson, S. E., Hibberson, W., & Ware, N. (1992). Origin of kimberlites and related magmas. *Earth and Planetary Science Letters*, *113*, 521–538.

Rudnick, R. L., & Gao, S. (2003). Composition of the continental crust. *Treatise on Geochemistry*, *3*, 1–64. https://doi.org/10.1016/b0-08-043751-6/03016-4

Scowen, P. A. H., Roeder, P. L., & Helz, R. T. (1991). Reequilibration of chromite within Kilauea Iki lava lake, Hawaii. *Contributions to Mineralogy and Petrology*, *107*, 8–20. https://doi.org/10.1007/bf00311181

Shishkina, T. A., Botcharnikov, R. E., Holtz, F., Almeev, R. R., & Portnyagin, M. V. (2010). Solubility of H_2O^- and CO_2-bearing fluids in tholeiitic basalts at pressures up to 500MPa. *Chemical Geology*, *277*, 115–125. https://doi.org/10.1016/j.chemgeo.2010.07.014

Sobolev, A. V., Hofmann, A. W., Kuzmin, D. V., Yaxley, G. M., Arndt, N. T., Chung, S.-L., et al. (2007). The amount of recycled crust in sources of mantle-derived melts. *Science*, *316*, 412–417.

Storey, B. C. (1995). The role of mantle plumes in continental breakup: Case histories from Gondwanaland. *Nature*, *377*, 301–308. https://doi.org/10.1038/377301a0

Storey, B. C., & Kyle, P. R. (1997). An active mantle mechanism for Gondwana breakup. *South African Journal of Geology*, *100*, 283–290.

Svensen, H., Corfu, F., Polteau, S., Hammer, Ø., & Planke, S. (2012). Rapid magma emplacement in the Karoo Large Igneous Province. *Earth and Planetary Science Letters*, *325–326*, 1–9. https://doi.org/10.1016/j.epsl.2012.01.015

Sweeney, R. J., Duncan, A. R., & Erlank, A. J. (1994). Geochemistry and petrogenesis of Central Lebombo basalts of the Karoo Igneous Province. *Journal of Petrology*, *35*, 95–125. https://doi.org/10.1093/petrology/35.1.95

Tainton, K. M., & McKenzie, D. (1994). The generation of kimberlites, lamproites, and their source rocks. *Journal of Petrology*, *35*, 787–817. https://doi.org/10.1093/petrology/35.3.787

Tappe, S., Smart, K., Torsvik, T., Massuyeau, M., & de Wit, M. (2018). Geodynamics of kimberlites on a cooling Earth: Clues to plate tectonic evolution and deep volatile cycles. *Earth and Planetary Science Letters*, *484*, 1–14. https://doi.org/10.1016/j.epsl.2017.12.013

Turunen, S. T., Luttinen, A. V., Heinonen, J. S., & Jamal, D. L. (2019). Luenha picrites, Central Mozambique-Messengers from a mantle plume source of Karoo continental flood basalts? *Lithos*, *346–347*, 105152. https://doi.org/10.1016/j.lithos.2019.105152

Ulmer, P. (1989). The dependence of the Fe^{2+}-Mg cation-partitioning between olivine and basaltic liquid on pressure, temperature and composition. *Contributions to Mineralogy and Petrology*, *101*, 261–273. https://doi.org/10.1007/bf00375311

White, W. M. (2010). Oceanic island basalts and mantle plumes: The geochemical perspective. *Annual Review of Earth and Planetary Sciences*, *38*, 133–160. https://doi.org/10.1146/annurev-earth-040809-152450

White, W. M. (2020). *Geochemistry* (2nd ed., 960 pp.). New York, NY: Wiley-Blackwell.

Wyatt, B. A., Baumgartner, M., Anckar, E., & Grutter, H. (2004). Compositional classification of "kimberlitic" and "non-kimberlitic" ilmenite. *Lithos*, *77*, 819–840. https://doi.org/10.1016/j.lithos.2004.04.025

Zhou, M.-F., Arndt, N. T., Malpas, J., Wang, C. Y., & Kennedy, A. K. (2008). Two magma series and associated ore deposit types in the Permian Emeishan large igneous province, SW China. *Lithos*, *103*, 352–368. https://doi.org/10.1016/j.lithos.2007.10.006